Efficient wide-range calculation of free energies in solids and liquids using reversible-scaling molecular dynamics

John A. Moriarty[1] and Justin B. Haskins[2]

[1]*Condensed Matter and Materials Division, Lawrence Livermore National Laboratory, Livermore, California 94551-0808, USA*

[2]*NASA-Ames Research Center, Moffett Field, California 94035, USA*

(Received 27 February 2014; revised manuscript received 22 July 2014; published 22 August 2014)

We elaborate a novel and efficient method to obtain multiphase Helmholtz free energies from molecular dynamics (MD) simulations over wide ranges of volume and temperature in materials that can be described by temperature-independent ion forces, with both higher accuracy and order-of-magnitude cost savings compared to direct thermodynamic-integration techniques. Our method leverages and significantly extends the technique of reversible-scaling molecular dynamics (RSMD) proposed by de Koning *et al.* [Phys. Rev. Lett. **83**, 3973 (1999)], which allows a free-energy difference in a given phase at constant volume to be calculated as a function of temperature from a single MD simulation. In mechanically stable solid phases, our approach carefully combines quasiharmonic lattice dynamics at low temperatures with an accurate and fully isolated RSMD simulation of the anharmonic vibrational free energy at high temperatures to produce a seamless free energy from zero temperature to above melt along constant-volume isochores. In the liquid, we combine a unique calculation of the free energy along a high-temperature reference isotherm with isochoric RSMD simulations from that temperature to below melt. In metastable solid phases that are mechanically unstable at low temperature, we use two-phase MD melt simulations together with the liquid free energy to obtain the solid free energy along the solidus melt line and then perform isochoric RSMD simulations to temperatures above and below that point. While our free-energy method is general, we have specifically adapted it here to the case of metals in which the ion forces are well described by model generalized pseudopotential theory (MGPT) multi-ion interatomic potentials, and additive electron-thermal free-energy contributions can be included. Then using refined Ta6.8x MGPT potentials, we have converged total free energies and their components to very high and unprecedented sub-milli-Rydberg (mRy) numerical accuracy in the stable-bcc, liquid, and metastable-fcc phases of tantalum for volumes ranging from up to 26% expansion to nearly twofold compression and for temperatures to 25 000 K. In turn, we have successfully used the free energies so obtained to calculate physically accurate thermodynamic properties and gain new insight into their behavior, including sensitive thermodynamic derivatives, bcc and fcc melt curves, and a multiphase equation of state for tantalum (Ta) over the same temperature range and for pressures as high as 600 GPa. We show that the anharmonic free-energy component in the bcc solid, although only 1–5 mRy in magnitude for Ta, can have a significant (15%–20%) effect on thermal expansivity, the Grüneisen parameter, and melt temperatures. We further show that the electron-thermal free-energy component can similarly impact the specific heat and thermal expansivity in both the solid and the liquid, while only minimally affecting (to$\leqslant$ 3%) the bcc and fcc melt curves.

DOI: 10.1103/PhysRevB.90.054113 PACS number(s): 05.70.Ce, 02.70.Ns, 34.20.Cf, 64.30.Ef

I. INTRODUCTION

The efficient calculation of accurate free energies in solids and liquids from molecular dynamics (MD) simulations is a challenging problem of longstanding interest and importance in condensed matter physics. Numerous specific computational schemes have been developed that depend to varying degrees on the principles of thermodynamic integration (TI) [1,2], adiabatic switching (AS) [2,3], and/or thermodynamic perturbation theory (TPT) [2,4,5]. Particularly challenging is the problem of efficiently calculating free energies in real materials over wide ranges of volume or pressure and temperature in multiple phases. This capability is required to obtain multiphase equations of state and equilibrium phase boundaries to high (1%–2%) accuracy from a given set of either quantum-mechanical or empirical interatomic forces. The simplifying and highly efficient method of reversible-scaling molecular dynamics (RSMD) proposed by de Koning *et al.* [3], which marries the principles of TI and AS, has proven to be useful in this regard, allowing one to obtain free-energy differences as a function of temperature at constant volume in a given phase from a single MD simulation. In their original paper, de Koning *et al.* [3] showed only that their RSMD technique could efficiently reproduce the classical free energy of a simple solid as obtained from TI. In a later paper, de Koning *et al.* [6] used the RSMD concept to develop a second single-simulation Clausius-Clapeyron integration (CCI) method that can be used to obtain the temperature-pressure phase boundary separating two phases, starting from a given initial temperature-pressure point on the boundary, and they successfully applied their CCI method to Lennard-Jones melting in argon.

While the CCI method is interesting in its own right, it still requires absolute free energies for both phases to establish a starting point on the phase boundary, and the CCI method does not produce free energies over the full volume/pressure and temperature landscapes of the phases treated. To address these more general needs, we have now extended the original RSMD method [3] and its application to obtain wide-ranging absolute free energies in solid, liquid, and metastable phases alike, smoothly joining the method to accurate absolute reference free-energy determination in

each phase. At the same time, we have fully integrated the RSMD method into the general quantum-based weak-coupling thermodynamic framework applicable to materials described by temperature-independent forces with additive zero-temperature, ion-thermal, and electron-thermal free-energy contributions. We have also pushed the computational limits of the method to achieve high numerical free-energy accuracy at reasonable cost, something that heretofore has generally not been possible with existing techniques.

In a given material, our generalized RSMD method can be applied to mechanically stable solid phases, to the liquid phase, and to metastable or stable high-temperature solid phases that are mechanically unstable at low temperature. In mechanically stable solid phases, we have been able to combine accurate RSMD simulation of the anharmonic vibrational free energy at high temperature with quasiharmonic lattice dynamics (QHLD) at low temperature to obtain an absolute and seamless free energy from zero temperature to above melt. In the corresponding liquid phase, we have similarly combined RSMD simulation of the ion-thermal free energy with a unique method to obtain an absolute reference free energy at high temperature, an approach developed by marrying the principles of AS and TPT. Using quantum-mechanical interatomic potentials obtained from model generalized pseudopotential theory (MGPT) [7–12], our free-energy approach applied to liquid and stable-solid phases has been successfully used to calculate high-pressure melt curves in metals [11,12] at higher accuracy and in a fraction of the time previously required from thermodynamic integration alone [8,9]. We have also extended our method to treat unstable solid phases that are only mechanically stabilized at high temperature by large anharmonic vibrational effects, where such structures become either metastable or stable phases in the high-temperature phase diagram [12]. The purpose of this paper is to elaborate the details of our generalized RSMD free-energy approach, and to illustrate the power and utility of the method through application to the temperature-pressure phase diagram and multiphase equation of state (EOS) of tantalum (Ta).

The present paper is intended as a planned complement to Ref. [12], which addressed the related issue of possible solid-phase polymorphism at high temperatures and pressures in Ta, using dynamic MD simulations via Z method [13] and two-phase coexistence [12,14] melt techniques to examine the thermodynamic phase stability of candidate solid phases relative to the bcc ground state. A preliminary bcc melt curve for Ta calculated with our RSMD free-energy method was introduced in Ref. [12], but it was only used there as a convenient baseline with which to test the accuracy of the Z and two-phase melt methods, with all RSMD-related details and further applications deferred to the present paper. In addition, it was shown in Ref. [12] that the Z method only produces an upper bound to the equilibrium melt curve, while the two-phase method is most accurate and reliable for large MD simulation cells. This underscores the importance of accurate and efficiently calculated free energies in treating the phase diagram and multiphase EOS.

To state more specifically the technical problem addressed in this paper, we seek to calculate the total Helmholtz free energy *per atom* $A(\Omega,T)$ for a given solid or liquid phase of a material over extended ranges of atomic volume Ω and temperature T in terms of the material's total internal energy,

$$E(\Omega,T) = -T^2 \left.\frac{\partial(A/T)}{\partial T}\right|_{\Omega}, \tag{1}$$

and total internal pressure,

$$P(\Omega,T) = -\left.\left(\frac{\partial A}{\partial \Omega}\right)\right|_{T}, \tag{2}$$

quantities that can be obtained directly from MD simulation at high temperature, and in the case of a mechanically stable solid phase from QHLD at low temperature. Formal thermodynamic integration of Eq. (1) from a reference temperature $T_{\rm ref}$ and Eq. (2) from a reference volume $\Omega_{\rm ref}$ gives, respectively,

$$A(\Omega,T) = (T/T_{\rm ref})A(\Omega,T_{\rm ref}) - T\int_{T_{\rm ref}}^{T}[E(\Omega,T')/(T')^2]dT' \tag{3}$$

and

$$A(\Omega,T) = A(\Omega_{\rm ref},T) - \int_{\Omega_{\rm ref}}^{\Omega} P(\Omega',T)d\Omega'. \tag{4}$$

Evaluating Eq. (4) at $T = T_{\rm ref}$ and inserting the result into Eq. (3) then yields

$$A(\Omega,T) = (T/T_{\rm ref})[A(\Omega_{\rm ref},T_{\rm ref}) - \int_{\Omega_{\rm ref}}^{\Omega} P(\Omega',T_{\rm ref})d\Omega'] - T\int_{T_{\rm ref}}^{T}[E(\Omega,T')/(T')^2]dT'. \tag{5}$$

Equation (5) is often the starting point for a direct TI calculation of $A(\Omega,T)$ from MD data on $E(\Omega,T)$ and $P(\Omega,T)$. This starting point has the advantage of requiring a reference free energy $A(\Omega_{\rm ref},T_{\rm ref})$ at only a single volume and temperature for a given phase. However, there are also unwanted computational inefficiencies in the integral terms in Eq. (5). Because pressure is inherently a derivative quantity, it is usually true that for a given level of computing effort, MD energies are obtained more accurately than pressures. For this reason, we prefer not to integrate the pressure to obtain a free-energy contribution, but instead to calculate the pressure after the fact from Eq. (2). This makes Eq. (3), which does not require knowledge of the pressure, a more attractive starting point than Eq. (5), although the former does require a reference free energy across an entire $T = T_{\rm ref}$ isotherm, or at least over some parametric curve $T_{\rm ref}(\Omega)$ that crosses the entire volume range of interest. Equations (3) and (5), however, still require a detailed knowledge of the total internal energy $E(\Omega,T)$ over the entire volume and temperature ranges of interest. In practice, this could easily require 50–100 long MD simulations to obtain $E(\Omega,T)$ accurately for a single wide-range phase. The simplification that RSMD provides is to replace the energy integral over temperature in Eqs. (3) and (5) with an equivalent time integral that can be evaluated in a single MD simulation.

Our generalized RSMD methodology to evaluate the free energy $A(\Omega,T)$ starting from Eq. (3) is developed in Sec. II for the relevant case of weak-coupling materials, whose thermodynamic functions can be partitioned into zero-temperature, ion-thermal and electron-thermal components, with assumed temperature-independent forces on the ions and small electron-thermal contributions. We derive a general RSMD equation

for the important ion-thermal free energy in Sec. II A, and then implement that result for the three material phases of most direct interest. First, in Sec. II B we treat the stable-solid phase, using a $T_{\rm ref} = 0$ reference isotherm, and including an accurate, isolated evaluation of the anharmonic vibrational contribution to the free energy, which can be directly added to the quasiharmonic contribution. Then in Sec. II C we address the liquid phase, using a high-temperature reference isotherm, and introducing an independent AS-TPT method to calculate the reference free energy along that isotherm. Finally, in Sec. II D we consider the metastable solid phase, using a reference high-temperature melt curve $T_{\rm m}(\Omega)$, which can be independently calculated by accurate two-phase MD coexistence simulations [12]. In Sec. II E we also discuss an efficient way to add the small additional electron-thermal free energy component for the case of metals.

While our developed free-energy methodology is general, and can be applied to metals and nonmetals alike, for definiteness and for the intended application to Ta in Sec. III, we have here specifically adapted the present methodology to the case of metals described by multi-ion MGPT interatomic potentials [7–12]. We have also taken this opportunity to elaborate additional important details in Sec. III A about our refined Ta6.8x MGPT potentials, which were first applied in Ref. [12]. As pointed out in Ref. [12], the Ta6.8x potentials represent a useful improvement to previous Ta4 MGPT potentials [9–11]. The Ta6.8x potentials are also considerably more accurate physically than earlier Ta3 potentials [9], which significantly overestimate bcc melt temperatures, as shown independently by Taioli *et al.* [15] and Haskins *et al*. [12]. The Ta3 potentials were previously used in Ref. [9] to address the bcc-liquid multiphase EOS in Ta, using direct TI to obtain free energies. The present Ta EOS applications in Sec. III are intended to fully supersede that work, while at the same time significantly extending the scope of the thermodynamic properties treated and providing new insight into their behavior.

With regard to the open question of other possible solid phases than bcc appearing in the equilibrium phase diagram of Ta, we have taken our basic guidance from the MGPT-MD studies in Ref. [12] and the previous quantum molecular dynamics (QMD) simulations of Burakovsky *et al.* [16], which both examined candidate A15, fcc, hcp, and hexagonal ω (hex-ω) phases. Special attention was paid in these studies to the hex-ω phase, which the small-cell QMD simulations [16] indicated was thermodynamically more stable than bcc at high temperature and pressures above 70 GPa. However, MGPT-MD simulations [12] showed that this was a size effect that vanished in the large-cell limit, and that below melt bcc was the stable-solid phase of Ta to at least 420 GPa. Furthermore, the MGPT-MD simulations directly showed that hex-ω exhibits poor mechanical stability and partial transformation to bcc, suggesting that it would actually be mechanically unstable at all temperatures and pressures in an unconstrained environment. The mechanical instability of hex-ω has since been so confirmed with first-principles, finite-temperature lattice-dynamics calculations [17,18]. Thus, of the structures studied in Refs. [12] and [16], only A15, fcc, and hcp remain as candidate metastable phases for our RSMD free-energy method. To that list additional candidate structures may be added in the future, including the orthorhombic *Pnma* structure, which recently has been predicted to be mechanically stable in Ta over wide ranges of temperature and pressure [17,18].

In the remainder of Sec. III, the Ta6.8x potentials are used to calculate the free energy and its components of the stable-bcc solid phase, the high-temperature liquid phase, and, as a prototype, the metastable-fcc phase of Ta. In the process, we test and challenge the computational accuracy and efficiency of our generalized RSMD free-energy method, as well as the physical accuracy of the Ta6.8x potentials, in describing both sensitive thermodynamic derivatives at ambient pressure and the equation of state and melt behavior of Ta at high pressure. The highly accurate treatment afforded by our free-energy method will also allow us to gain new insight into the roles of anharmonic and electron-thermal contributions to individual Ta properties. Our conclusions are given in Sec. IV.

II. THEORETICAL AND COMPUTATIONAL APPROACH

We assume that the thermodynamics of the system of interest is well described by the conventional weak-coupling model, in which the total Helmholtz free energy can be expressed as a sum of cold ($T = 0$), ion-thermal, and electron-thermal contributions:

$$A(\Omega,T) = E_0(\Omega) + A_{\rm ion}(\Omega,T) + A_{\rm el}(\Omega,T), \tag{6}$$

with corresponding equations for the total internal energy and pressure:

$$E(\Omega,T) = E_0(\Omega) + E_{\rm ion}(\Omega,T) + E_{\rm el}(\Omega,T), \tag{7}$$

$$P(\Omega,T) = P_0(\Omega) + P_{\rm ion}(\Omega,T) + P_{\rm el}(\Omega,T). \tag{8}$$

In Eq. (6) we have noted that one can take $A_0 = E_0$ and remain consistent with Eq. (3) without any loss in generality. It further follows that the ion-thermal and electron-thermal free-energy components, $A_{\rm ion}$ and $A_{\rm el}$ in Eq. (6), satisfy Eq. (3) separately:

$$A_{\rm ion}(\Omega,T) = (T/T_{\rm ref})A_{\rm ion}(\Omega,T_{\rm ref}) - T\int_{T_{\rm ref}}^{T}[E_{\rm ion}(\Omega,T')/(T')^2]dT', \tag{9}$$

$$A_{\rm el}(\Omega,T) = (T/T_{\rm ref})A_{\rm el}(\Omega,T_{\rm ref}) - T\int_{T_{\rm ref}}^{T}[E_{\rm el}(\Omega,T')/(T')^2]dT'. \tag{10}$$

Consistent with the requirements of RSMD simulation [3], Eqs. (6)–(10) also implicitly assume that the forces that control ion motion in the system are independent of temperature. In compatible quantum-mechanical treatments, such forces would normally be obtained at zero electron temperature, as for example, with first-principles generalized pseudopotential theory (GPT) [19–23] pair potentials, or *model* GPT (MGPT) [7–12] multi-ion potentials, or with tight-binding approaches such as Pettifor's bond-order potentials (BOP) [24–26]. In such a case, the final electron-thermal free-energy component $A_{\rm el}$ in Eq. (6) embodies the remaining effects of electron temperature $T_{\rm el}$ on the structure and occupation of the electronic states of the system. Quantum-mechanical treatments that

explicitly incorporate electron temperature and produce $T_{\rm el}$-dependent forces, however, such as QMD simulations in metals based on finite-temperature density-functional theory (DFT) [5,15,16,27], or the new $T_{\rm el}$-dependent MGPT potentials for transition metals [27], are currently beyond the scope of RSMD and are not directly considered here. At the other extreme, temperature-independent empirical potentials such as embedded-atom method (EAM) [28] or Finnis-Sinclair (FS) [29] potentials are compatible with RSMD and the present free-energy approach. The present approach has been specifically adapted to multi-ion MGPT potentials, but for suitable materials can be extended to GPT, BOP, EAM, FS, or any other temperature-independent potentials that will support RSMD simulations.

Two further practical considerations concerning the application of Eqs. (6)–(10) should also be mentioned. First, the cold energy and pressure components, E_0 and P_0, in Eqs. (6)–(8) can be treated in two closely related but distinct ways. The first option is to assign E_0 and P_0 to the $T = 0$ ground-state phase of the material and absorb the structural-energy differences with other phases into $A_{\rm ion}(\Omega,T_{\rm ref})$ in Eq. (9). This option is especially convenient when treating the liquid in combination with the ground state or other stable-solid phase to obtain an equilibrium melt curve, and is the treatment of choice for this case. Alternatively, one can calculate a separate E_0 and P_0 for each phase considered. This option is most useful when one is treating multiple solid phases, including metastable phases.

The second practical consideration here concerns the treatment of the electron-thermal free-energy component $A_{\rm el}$ in Eq. (6). In systems where the underlying weak-coupling thermodynamic model works well, $A_{\rm el}$ is a small correction to $A_{\rm ion}$, and this is implicitly assumed in the development below. If desired, $A_{\rm el}$ can be neglected entirely, as is usually done for semiconductors or insulators, or is often done for metals as well when the required electron-thermal information is not available. Alternatively, however, $A_{\rm el}$ can be treated in a separate approximate manner, as discussed below in Sec. II E for the case of metals. But for metals and nonmetals alike, the central focus of attention in the present approach is the calculation of the ion-thermal free-energy component $A_{\rm ion}$, to which the RSMD method is specifically addressed.

A. Reversible-scaling molecular dynamics for $A_{\rm ion}$

The RSMD approach of de Koning *et al.* [3] takes direct advantage of the fact that in the classical statistical mechanics of an MD simulation for an N-ion system, the free energy depends on the total potential-energy function $U(\mathbf{R}) \equiv U(\mathbf{R}_1,\mathbf{R}_2,\ldots,\mathbf{R}_N)$ establishing the interatomic forces on the ions only through the Boltzmann factor $\exp(-U/k_{\rm B}T)$, where $k_{\rm B}$ is the Boltzmann constant. If one runs an MD simulation at a fixed simulation temperature $T_{\rm ref}$ for a scaled potential-energy function λU, then the corresponding free energy of the unscaled system is thereby determined for a temperature $T = T_{\rm ref}/\lambda$. In an RSMD simulation, the scaling factor λ is allowed to vary slowly and linearly with time,

$$\lambda(t) = 1 + \frac{\lambda_f - 1}{t_S}t, \tag{11}$$

starting from an initial value of $\lambda = 1$, corresponding to the initial temperature $T_{\rm ref}$, to a final value of $\lambda_f = \lambda(t_S) = T_{\rm ref}/T_f$, where T_f is the final apparent temperature for which the free energy is to be obtained. If the switching time t_S between those limits is long, then the RSMD simulation process is adiabatic and the temperature integral in Eq. (9) can be evaluated in terms of an equivalent time integral $W_{\rm ion}$ [3] as follows:

$$-T\int_{T_{\rm ref}}^{T}[E_{\rm ion}(\Omega,T')/(T')^2]dT' = \frac{W_{\rm ion}}{\lambda} + \frac{3}{2}k_BT\,\ln\lambda - \left(1-\frac{1}{\lambda}\right)E_0, \tag{12}$$

where

$$W_{\rm ion}[\Omega,T(t)] = \frac{1}{N}\int_0^t \frac{d\lambda(t')}{dt'}U[\mathbf{R}(t')]dt' = \frac{1}{N}\frac{\lambda_f - 1}{N_S}\sum_{n=1}^{n_S(t)}U[\mathbf{R}(t_n)]. \tag{13}$$

In the second line of Eq. (13), the time integral has been evaluated using the histogram method, assuming a small simulation time step h and N_S time steps, such that $t_S = N_S h$. In practice we take h on the order of 0.2 fs and N_S in the range 10^5–10^7, depending on the problem addressed and the numerical accuracy required, so t_S is in the range of 20–2000 ps. Finally, inserting Eq. (12) back into Eq. (9) and using $\lambda^{-1} = T/T_{\rm ref}$ one has the general result

$$A_{\rm ion}(\Omega,T) = \frac{T}{T_{\rm ref}}[E_0(\Omega) + A_{\rm ion}(\Omega,T_{\rm ref}) + W_{\rm ion}(\Omega,T)] - \frac{3}{2}k_{\rm B}T\,\ln\frac{T}{T_{\rm ref}} - E_0(\Omega). \tag{14}$$

The use of this result in the special cases of the stable solid, the liquid, and the metastable solid is discussed below in Secs. II B, II C, and II D, respectively.

B. Ion-thermal free energy $A_{\rm ion}^{\rm sol}$ of the stable solid

The ion-thermal free energy for a stable-solid phase can be conveniently divided into quasiharmonic and anharmonic contributions:

$$A_{\rm ion}^{\rm sol}(\Omega,T) = A_{\rm ion}^{\rm qh}(\Omega,T) + A_{\rm ion}^{\rm ah}(\Omega,T). \tag{15}$$

The former contribution can be expressed directly in terms of the volume-dependent quasiharmonic phonon frequencies $\nu_\lambda(\mathbf{q},\Omega)$ of the solid crystal structure in question by the well-known result

$$A_{\rm ion}^{\rm qh}(\Omega,T) = \frac{k_{\rm B}T}{N}\sum_{\mathbf{q},\lambda}\ln\{2\,\sinh[h\nu_\lambda(\mathbf{q},\Omega)/(2k_{\rm B}T)]\}, \tag{16}$$

where the sum is over all wave vectors $\mathbf{q}$ and phonon branches λ in the first Brillouin zone (BZ) of the reciprocal lattice. Equation (16) fully takes into account the quantum Bose-Einstein statistics required in the low-temperature solid and is consistent with a $T_{\rm ref} = 0$ reference temperature, such that

$A^{\rm qh}_{\rm ion}(\Omega,0) = E^0_{\rm ph}(\Omega)$, where

$$E^0_{\rm ph}(\Omega) = \frac{1}{2N}\sum_{\mathbf{q},\lambda} h\nu_\lambda(q,\Omega) \tag{17}$$

is the zero-point vibrational energy.

The corresponding anharmonic free-energy contribution $A^{\rm qh}_{\rm ion}$ can be obtained from the RSMD result for $A_{\rm ion}$, Eq. (14), in the following manner. Equation (14) is based on classical Boltzmann statistics and from that equation one must subtract the corresponding classical harmonic component of the ion free energy, $3k_{\rm B}T(1-\ln T)$. Assuming only that $A^{\rm ah}_{\rm ion}(\Omega,T_{\rm ref}) = 0$, so that $A_{\rm ion}(\Omega,T_{\rm ref}) = 3k_{\rm B}T_{\rm ref}(1-\ln T_{\rm ref})$ in Eq. (14), one is left with an isolated, explicit equation for the anharmonic free energy:

$$A^{\rm ah}_{\rm ion}(\Omega,T) = \frac{T}{T_{\rm ref}}[E_0(\Omega) + W_{\rm ion}(\Omega,T)] + \frac{3}{2}k_{\rm B}T\,\ln\frac{T}{T_{\rm ref}} - E_0(\Omega). \tag{18}$$

We note that physically the anharmonic free energy will vanish at zero temperature, so that $A^{\rm ah}_{\rm ion}(\Omega,0) = 0$, and further that $A^{\rm ah}_{\rm ion}$ remains negligibly small for temperatures below the Debye temperature, $T < \Theta_{\rm D}$. On the other hand, as a practical matter RSMD simulation cannot be carried down to very low temperatures and is most efficient and accurate numerically when $T \geqslant T_{\rm ref} > \Theta_{\rm D}$. As a compromise, we assume a volume-dependent reference temperature in Eq. (18) of the form $T_{\rm ref}(\Omega) = x_{\rm D}\Theta_{\rm D}(\Omega)$, where $x_{\rm D}$ is a chosen fixed parameter and the Debye temperature is defined by the equation

$$k_{\rm B}\Theta_{\rm D}(\Omega) = \tfrac{8}{9}E^0_{\rm ph}(\Omega). \tag{19}$$

In practice, we find that an optimum choice for $x_{\rm D}$ is in the range $0.5 \leqslant x_{\rm D} \leqslant 0.8$. For such a choice, $A^{\rm ah}_{\rm ion}(\Omega,T)$ can be evaluated as a function of temperature at a given volume using Eq. (18) and a single RSMD simulation ranging from $T = x_{\rm D}\Theta_{\rm D}$ to $T = T^{\rm sol}_{\rm max}$, the maximum temperature of interest in the solid at that volume. To maintain good physical accuracy, $T^{\rm sol}_{\rm max}$ should not be taken too far above the solidus melt point, which can be estimated for this purpose by the volume-dependent Lindemann melt temperature

$$T_{\rm L}(\Omega) = T^0_{\rm m}\big[\Theta_{\rm D}(\Omega)/\Theta_{\rm D}\big(\Omega^0_{\rm m}\big)\big]^2\big(\Omega/\Omega^0_{\rm m}\big)^{2/3}, \tag{20}$$

with $T^0_{\rm m}$ the observed or calculated stable-solid melt temperature at solidus volume $\Omega^0_{\rm m}$. One can then take $T^{\rm sol}_{\rm max}(\Omega) = x^{\rm max}_{\rm L}T_{\rm L}(\Omega)$, with $x^{\rm max}_{\rm L}$ a chosen parameter in the range $1 \leqslant x^{\rm max}_{\rm L} \leqslant 2$, depending on the magnitude of $T_{\rm L}$. At expanded volumes, where $T_{\rm L}$ is small, a value in the vicinity of $x^{\rm max}_{\rm L} = 2$ can be safely used, while at high pressure, where $T_{\rm L}$ is large, a value near $x^{\rm max}_{\rm L} = 1$ is usually required.

C. Ion-thermal free energy $A^{\rm liq}_{\rm ion}$ of the liquid

In the liquid, Eq. (14) can be used directly to obtain the temperature dependence of $A^{\rm liq}_{\rm ion}$, but the challenge is to independently calculate the required reference free energy $A^{\rm liq}_{\rm ion}(\Omega,T_{\rm ref})$ in an accurate and efficient manner. To do this, we take $T_{\rm ref}$ to be a high temperature at the top of the range of interest in the liquid, $T_{\rm ref} = T^{\rm liq}_{\rm max}$, and well above the maximum expected melt temperature in the volume range of interest. We next introduce an appropriate reference system, with potential-energy function $U_{\rm ref}(\mathbf{R})$, whose free energy $A^{\rm ref}_{\rm ion}(\Omega,T_{\rm ref})$ is accurately known at the required conditions. The principle of adiabatic switching then allows one to calculate $A_{\rm ion}(\Omega,T_{\rm ref})$ with equal accuracy by a smooth thermodynamic integration from the reference system to the true system:

$$A^{\rm liq}_{\rm ion}(\Omega,T_{\rm ref}) = A^{\rm ref}_{\rm ion}(\Omega,T_{\rm ref}) + \frac{1}{N}\int_0^1 \langle U(\mathbf{R}) - U_{\rm ref}(\mathbf{R})\rangle_\lambda d\lambda, \tag{21}$$

where here λ is a scaling parameter varying between 0 and 1, and the quantity $\langle U(\mathbf{R}) - U_{\rm ref}(\mathbf{R})\rangle_\lambda$ in the integrand is a thermal average at volume Ω and temperature $T_{\rm ref}$ in the canonical ensemble of the mixed potential-energy function

$$U_\lambda(\mathbf{R}) = \lambda U(\mathbf{R}) + (1-\lambda)U_{\rm ref}(\mathbf{R}). \tag{22}$$

To make the integration in Eq. (21) computationally efficient, however, the reference system used must be a good match to the physical system under consideration, so that $\langle U(\mathbf{R}) - U_{\rm ref}(\mathbf{R})\rangle_\lambda = \langle dU_\lambda/d\lambda\rangle_\lambda$ varies slowly and smoothly as a function of λ, and only a few points are needed to evaluate the integral accurately.

In most materials, the thermodynamics of the high-temperature liquid is dominated by short-range repulsive forces, and a useful reference system to consider in the context of Eq. (21) is the inverse 12th power potential, r^{-12}, a potential that has been extensively studied via computer simulations and for which an accurate free energy and pair-correlation function are known [30]. This choice also allows one to use the powerful technique of TPT to optimize the coefficient of the potential. Specifically, for weak-coupling liquid metals at high temperature, where the potential-energy function $U(\mathbf{R})$ can be approximated in the general form

$$U(\mathbf{R}) \approx \bar{U}(\mathbf{R}) = NE_{\rm vol}(\Omega) + \frac{1}{2}{\sum_{i,j}}' v^{\rm eff}_2(R_{ij},\Omega), \tag{23}$$

a special version of TPT, known as variational perturbation theory (VPT) [4,8,30,31], provides a rigorous upper bound (ub) on the liquid free energy $A_{\rm liq}$ (in the limit $A_{\rm el} = 0$):

$$A_{\rm liq}(\Omega,T) \equiv E_0(\Omega) + A^{\rm liq}_{\rm ion}(\Omega,T) \leqslant A^{\rm ub}_{\rm liq}(\Omega,T), \tag{24}$$

where

$$A^{\rm ub}_{\rm liq}(\Omega,T) = E_{\rm vol}(\Omega) + A_{\rm ref}(z,T) + (2\pi/\Omega) \times \int_0^\infty g_{\rm ref}(r,z)\big[v^{\rm eff}_2(r,\Omega) - v_{\rm ref}(r,z)\big]r^2dr. \tag{25}$$

In Eqs. (23) and (25), $E_{\rm vol}$ is a structure-independent volume term and $v^{\rm eff}_2$ is a volume-dependent effective pair potential for the true system, while $A_{\rm ref}$, $g_{\rm ref}$, and $v_{\rm ref}$ are, respectively, the free energy, pair-correlation function, and pair potential of the r^{-12} reference system [30], with

$$A_{\rm ref}(z,T) = \sum_{n=1}^{5}\frac{1}{n}B_{n+1}z^nk_{\rm B}T + A_{\rm gas}(\Omega,T), \tag{26}$$

$$v_{\rm ref}(r,z) = \varepsilon(\sigma/r)^{12}, \tag{27}$$

and $z = (\sigma^3/\sqrt{2}\Omega)(\varepsilon/k_B T)^{1/4}$. In Eq. (26) the B_{n+1} are the calculated virial coefficients: $B_2 = 3.6296$, $B_3 = 7.5816$, $B_4 = 9.9792$, $B_5 = 8.4520$, and $B_6 = 4.4$; while $A_{\rm gas}$ is the ideal-gas free energy: $A_{\rm gas}(\Omega,T) = -[\ln(\Omega/\lambda_{\rm ion}^3) + 1]k_B T$, with $\lambda_{\rm ion} = \sqrt{(2\pi\hbar^2)/(M_{\rm ion}k_B T)}$ and $M_{\rm ion}$ the ion mass.

At each of the volumes of interest and temperature $T = T_{\rm ref}$, the variational parameter z can be chosen to minimize the right-hand side of Eq. (25), yielding a function $z^{\rm ub}(\Omega)$, for which $A_{\rm liq}^{\rm ub}(\Omega,T_{\rm ref})$ becomes a close upper bound to the true liquid free energy $A_{\rm liq}(\Omega,T_{\rm ref})$ over the entire volume range. A corresponding lower bound (lb) on the free energy can also be established by VPT [31]:

$$A_{\rm liq}(\Omega,T) \geqslant A_{\rm liq}^{\rm lb}(\Omega,T), \tag{28}$$

where

$$A_{\rm liq}^{\rm lb}(\Omega,T) = E_{\rm vol}(\Omega) + A_{\rm ref}(z) + (2\pi/\Omega) \times \int_0^\infty g_{\rm eff}(r,\Omega)[v_2^{\rm eff}(r,\Omega) - v_{\rm ref}(r,z)]r^2 dr. \tag{29}$$

In Eq. (29), $g_{\rm eff}(r,\Omega)$ is the true-system pair-correlation function for $v_2^{\rm eff}(r,\Omega)$ and must be determined from independent MD simulations at the volumes of interest and $T = T_{\rm ref}$. The variational parameter z can now be chosen to maximize the right-hand side of Eq. (28) at each volume, yielding $z^{\rm lb}(\Omega)$ and making $A_{\rm liq}^{\rm lb}(\Omega,T_{\rm ref})$ a close lower bound to $A_{\rm liq}(\Omega,T_{\rm ref})$ across the volume range.

An approximate baseline value for $A_{\rm ion}^{\rm liq}(\Omega,T_{\rm ref})$ can be calculated by simply averaging the upper and lower bounds of $A_{\rm liq}(\Omega,T_{\rm ref})$ and then subtracting the cold energy:

$$A_{\rm ion}^{\rm liq}(\Omega,T_{\rm ref}) \cong \tfrac{1}{2}\left[A_{\rm liq}^{\rm ub}(\Omega,T_{\rm ref}) + A_{\rm liq}^{\rm lb}(\Omega,T_{\rm ref})\right] - E_0(\Omega). \tag{30}$$

While Eq. (30) often provides a good estimate, the more reliable and accurate procedure to obtain $A_{\rm ion}^{\rm liq}(\Omega,T_{\rm ref})$ is to calculate first the average of $z^{\rm ub}$ and $z^{\rm lb}$,

$$\bar{z}(\Omega) = \tfrac{1}{2}[z^{\rm ub}(\Omega) + z^{\rm lb}(\Omega)], \tag{31}$$

and then use this result to define the final details of the r^{-12} reference system to be used in Eq. (21) for $A_{\rm ion}^{\rm liq}(\Omega,T_{\rm ref})$. One thereby has as input for Eq. (21)

$$A_{\rm ion}^{\rm ref}(\Omega,T_{\rm ref}) = A_{\rm ref}(\bar{z},T_{\rm ref}) \tag{32}$$

and

$$U_{\rm ref}(\mathbf{R}) = \frac{1}{2}{\sum_{i,j}}' v_{\rm ref}(R_{ij},\bar{z}) = \frac{1}{2}{\sum_{i,j}}' \frac{4(\bar{z}\Omega)^4 k_B T_{\rm ref}}{R_{ij}^{12}}, \tag{33}$$

with $A_{\rm ref}$ given by Eq. (26). It should also be noted in this regard that the approximate form of $U(\mathbf{R}) \approx \bar{U}(\mathbf{R})$ assumed in Eq. (23) is used here only to obtain $\bar{z}$, and that once $\bar{z}$ is calculated, the full potential-energy function $U(\mathbf{R})$ is to be used in Eq. (21). The construction of $\bar{U}(\mathbf{R})$ from $U(\mathbf{R})$ will be discussed below in Sec. III B for the case of transition metals described by multi-ion MGPT potentials.

Once the reference free energy $A_{\rm ion}^{\rm liq}(\Omega,T_{\rm ref})$ has been established for use in Eq. (14), that equation can be used directly to calculate the liquid ion-thermal free energy $A_{\rm ion}^{\rm liq}(\Omega,T)$ as a function of temperature at given volume from the chosen reference temperature $T = T_{\rm ref} = T_{\rm max}^{\rm liq}$ down to some desired minimum temperature $T = T_{\rm min}^{\rm liq}$ below the melt curve. It is again very often convenient to express the latter temperature as a specific fraction $x_{\rm L}^{\rm min}$ of the volume-dependent Lindemann melt temperature, such that $T_{\rm min}^{\rm liq}(\Omega) = x_{\rm L}^{\rm min} T_{\rm L}(\Omega)$. The optimum value of $x_{\rm L}^{\rm min}$ depends to some extent on the application at hand. For melting from the stable-solid phase, a value in the range $0.5 \leqslant x_{\rm L}^{\rm min} \leqslant 0.8$ usually works well.

D. Ion-thermal free energy $A_{\rm ion}^{\rm sol}$ of the metastable solid

Metastable solid phases that are fully mechanically stable at low temperature with all real $T = 0$ phonon frequencies present no special problem, and such cases can be treated in the same manner as the stable-solid phase discussed in Sec. II B above. The challenging case is that of a metastable phase that is mechanically unstable at low temperature and is only mechanically stabilized at high temperature by anharmonic phonon-phonon interactions, with or without the aid of additional electron-thermal effects. Such a phase has at least some imaginary phonon frequencies at $T = 0$, and hence its quasiharmonic ion-thermal free energy, $A_{\rm ion}^{\rm qh}$ as given by Eq. (16), does not exist and cannot be used to establish the reference energy $A_{\rm ion}^{\rm sol}(\Omega,T_{\rm ref})$ that is required in Eq. (14). For this case we have developed a special procedure to determine $A_{\rm ion}^{\rm sol}(\Omega,T_{\rm ref})$ along the solidus melt line of the metastable phase in the $A_{\rm el} = 0$ limit. In that limit, the melt curve for the metastable phase can be determined directly by MD simulation using an accurate two-phase coexistence method [12,27]. From the two-phase melt calculation, one can extract the volume-dependent reference solidus melt temperature $T_{\rm m}^{\rm sol}(\Omega)$, melt pressure $P_{\rm m}^{\rm sol}(\Omega)$, and melt energy $E_{\rm m}^{\rm sol}(\Omega)$ over the entire volume range of interest. Along the melt line, the melt temperature $T_{\rm m}$, melt pressure $P_{\rm m}$, and Gibbs free energy, $G = A + P\Omega$, of the liquid and of the metastable solid must be equal, so that $P_{\rm m} = P_{\rm m}^{\rm sol} = P_{\rm m}^{\rm liq}$, $T_{\rm m} = T_{\rm m}^{\rm sol} = T_{\rm m}^{\rm liq}$, and the Helmholtz free energy of the metastable solid along the solidus melt line can be calculated as

$$A_{\rm sol}(\Omega_{\rm sol},T_{\rm m}) = A_{\rm liq}(\Omega_{\rm liq},T_{\rm m}) + P_{\rm m}(\Omega_{\rm liq} - \Omega_{\rm sol}). \tag{34}$$

For given values of $T_{\rm m}$, $P_{\rm m}$, and the solidus volume $\Omega_{\rm sol}$ on the melt curve, the corresponding liquidus volume $\Omega_{\rm liq}$ and free energy $A_{\rm liq}(\Omega_{\rm liq},T_{\rm m})$ can be obtained via interpolation on the liquid equation of state (calculated in the $A_{\rm el} = 0$ limit). With $T_{\rm ref} = T_{\rm m}$ and $\Omega = \Omega_{\rm sol}$, Eq. (34) can be used directly to establish the reference energy

$$A_{\rm ion}^{\rm sol}(\Omega,T_{\rm ref}) = A_{\rm sol}(\Omega_{\rm sol},T_{\rm m}) - E_0(\Omega_{\rm sol}) \tag{35}$$

needed in Eq. (14). One can then apply Eq. (14) both upward in temperature from $T = T_{\rm m}$ to the desired maximum $T = T_{\rm max}^{\rm sol}$ and downward in temperature from $T = T_{\rm m}$ to an allowable minimum $T = T_{\rm min}^{\rm sol}$, which must be established independently for the metastable phase in question. Once $A_{\rm ion}^{\rm sol}(\Omega,T)$ is thereby calculated for the volumes and temperatures of interest, the electron-thermal component $A_{\rm el}(\Omega,T)$ can finally be added to it to establish a total free energy and equation of state for the metastable phase.

E. Electron-thermal free energy A_{el} in metals

For metals, the simplest treatment of the additional electron-thermal contribution to the thermodynamics is to use the standard low-temperature expansion of the total internal energy $E(\Omega,T)$ to obtain the leading T^2 contribution to $E_{el}(\Omega,T)$. Inserting the latter contribution into Eq. (10) with $T_{ref}=0$, one then recovers the well-known result

$$A_{e1}(\Omega,T) = -E_{e1}(\Omega,T) = -\frac{\pi^2}{6}(k_B T)^2\,\rho(E_F), \qquad (36)$$

where $\rho(E_F)$ is the $T=0$ density of electronic states at the Fermi level. This treatment is usually adequate in simple metals, where the structure dependence to the density of states is weak and $\rho(E_F)$ can be well approximated by a free-electron form. In transition metals, however, $\rho(E_F)$ is strongly material and structure dependent, so Eq. (36) is only adequate up to modest temperatures in the solid ground-state phase. A more accurate treatment of A_{el} and E_{el} for high-temperature transition-metal phases has been developed in terms of configuration-averaged, finite-temperature DFT calculations of the electronic entropy $S_{el} = -\partial A_{el}/\partial T$ in the hot solid and liquid, using atomic configurations obtained from MGPT-MD simulations [9]. In the prototype case of Ta, the DFT values of electronic entropy thereby obtained in both the hot solid and the liquid can be well fit in the form

$$S_{el}(\Omega,T) = \alpha(\Omega)T + \gamma(\Omega)T^3 + \cdots, \qquad (37)$$

so that

$$A_{el}(\Omega,T) = -\tfrac{1}{2}\alpha(\Omega)T^2 - \tfrac{1}{4}\gamma(\Omega)T^4 + \cdots \qquad (38)$$

and

$$E_{el}(\Omega,T) = \tfrac{1}{2}\alpha(\Omega)T^2 + \tfrac{3}{4}\gamma(\Omega)T^4 + \cdots. \qquad (39)$$

In the vicinity of melt for Ta, the resulting A_{el} and E_{el} functions differ little in the hot solid and the liquid, and these functions can be adequately approximated by only the first expansion term in Eqs. (38) and (39), respectively. In that limit, one recovers the form of Eq. (36), but with $\rho(E_F)$ replaced by an effective volume-dependent density of states $\rho_{eff}(\Omega) = 3\alpha(\Omega)/(\pi k_B)^2$. Even then, the electron-thermal contribution has been found to lower the calculated melt curve in Ta by only a small amount (<5%) [9–12]. At the same time, the electron-thermal contribution to sensitive thermodynamic derivatives such as the specific heat and the thermal expansion coefficient can be much larger, as we specifically demonstrate for Ta in Sec. III.

III. APPLICATION TO TANTALUM

In this section we consider the application of the generalized RSMD free-energy methodology described in Sec. II above to the high-pressure phase diagram and multiphase equation of state of Ta, as determined by the present Ta6.8x MGPT interatomic potentials and additional electron-thermal contributions. Our treatment will include both ambient and extreme conditions, with the latter extending to as high as 600 GPa in pressure and to 25 000 K in temperature.

A. Ta6.8x MGPT interatomic potentials

Within DFT quantum mechanics, GPT provides a first-principles approach to multi-ion interatomic potentials in d-band transition metals [32], with the real-space total-energy functional for the bulk material obtained at $T_{el}=0$ in the general form

$$E_{tot}(\mathbf{R};\Omega) = N E_{vol}(\Omega) + \frac{1}{2}{\sum_{i,j}}' v_2(ij;\Omega) + \frac{1}{6}{\sum_{i,j,k}}' v_3(ijk;\Omega) + \frac{1}{24}{\sum_{i,j,k,l}}' v_4(ijkl;\Omega), \qquad (40)$$

where the prime on each summation sign indicates the exclusion of all self-interaction terms from the summation. The leading volume term E_{vol} in Eq. (40), as well as the two-ion pair potential v_2 and the three- and four-ion angular-force potentials v_3 and v_4 depend explicitly on the atomic volume Ω but are structure independent and transferable to all bulk ion configurations, either ordered or disordered. The simplified *model* GPT or MGPT [7–12] derives from the GPT through a series of systematic approximations applied to E_{vol} and the potentials v_n, approximations that are valid for mid-period transition metals with nearly half-filled d bands. These two main approximations are (i) the neglect of explicit sp-d hybridization contributions to the potentials v_n, contributions which destructively interfere for half-filled d bands; and (ii) the introduction of highly symmetrical canonical d bands [7], which allow the remaining d-state band-structure contributions to the potentials to be evaluated analytically in terms of a single radial function $f(r)$ and three universal angular functions, L, P, and M, that depend only on d symmetry.

In the MGPT, the two-ion pair potential consists of four main contributions:

$$v_2(r,\Omega) = v_2^{sp}(r,\Omega) + v_2^{hc}(r,\Omega) + v_a(\Omega)[f(r)]^4 - v_b(\Omega)[f(r)]^2, \qquad (41)$$

where v_2^{sp} is a pseudopotential-derived screened ion-ion potential for the s and p valence electrons; v_2^{hc} is a repulsive "hard-core" potential, arising mainly from d-state nonorthogonality effects; and v_a and v_b are volume-dependent coefficients for the direct d-band contributions. In the latter two terms, $f(r) = (1.8R_{WS}/r)^p$, where R_{WS} is the Wigner-Seitz radius and p is a weakly volume-dependent parameter, with a Gaussian cutoff introduced into $f(r)$ beyond the bcc second-neighbor distance [33]. For ideal canonical d bands, $p = 2\ell+1 = 5$ with $\ell = 2$, but in all Ta applications, including the present Ta6.8x potentials, we have taken $p=4$ at the observed equilibrium volume $\Omega_0 = 121.6$ a.u., and then allowed p to increase monotonically for decreasing Ω, as shown in Fig. 1(a).

The angular-force multi-ion potentials v_3 and v_4 in Eq. (40) reflect directional bonding contributions arising from partial d-band filling, and in the MGPT these potentials are given by corresponding multi-ion d-band functions, which can be expressed in terms of three and six radial distances,

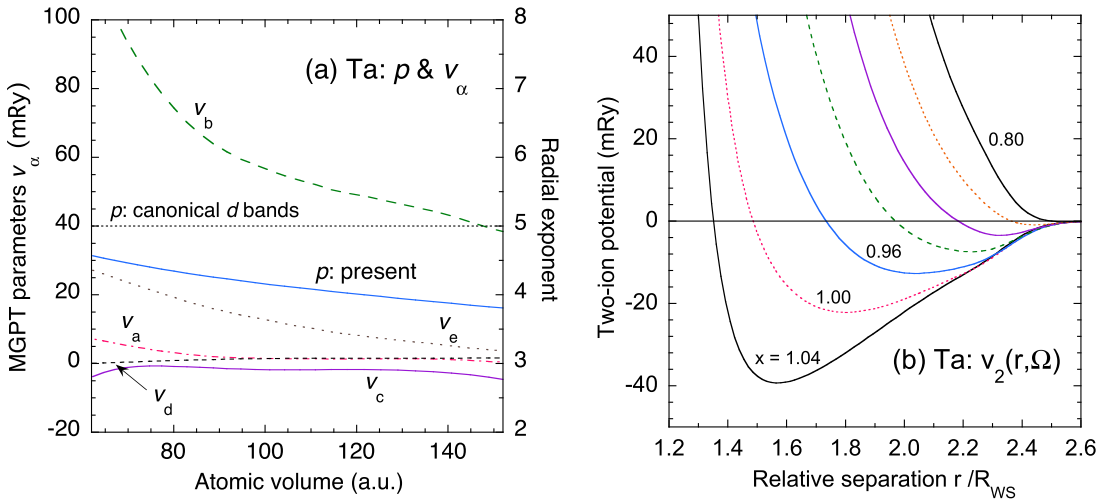

FIG. 1. (Color online) Volume dependence of the MGPT potential parameters and pair potential for Ta6.8x. (a) Radial function exponent p for $f(r)$ (right vertical scale) and d-band potential coefficients v_α (left vertical scale). (b) Two-ion pair potential v_2 for selected volumes, in x increments of 0.04 with $x = (\Omega/\Omega_0)^{1/3}$.

r_n, respectively, and dependent angles, θ_n:

$$v_3(r_1,r_2,r_3;\Omega) = v_c(\Omega)f(r_1)f(r_2)f(r_3)L(\theta_1,\theta_2,\theta_3) + v_d(\Omega)\{[f(r_1)f(r_2)]^2P(\theta_3) + [f(r_2)f(r_3)]^2P(\theta_1)+[f(r_3)f(r_1)]^2P(\theta_2)\} \quad (42)$$

and

$$v_4(r_1,r_2,r_3,r_4,r_5,r_6;\Omega) = v_e(\Omega)[f(r_1)f(r_2)f(r_3)f(r_4)M(\theta_1,\theta_2,\theta_3,\theta_4,\theta_5,\theta_6) + f(r_3)f(r_2)f(r_6)f(r_5)M(\theta_7,\theta_8,\theta_9,\theta_{10},\theta_5,\theta_{12}) + f(r_1)f(r_6)f(r_4)f(r_3)M(\theta_{11},\theta_{12},\theta_5,\theta_6,\theta_3,\theta_4)], \quad (43)$$

where v_c, v_d, and v_e are additional volume-dependent d-band coefficients. The specific three- and four-ion geometries assumed in Eqs. (42) and (43) are defined in Figs. 4(a) and 6, respectively, of Ref. [7].

In the MGPT, the two-ion potential contributions v_2^{sp} and $v_2^{\rm hc}$ in Eq. (41) are determined from first-principles, as in the full GPT. The remaining five d-band coefficients v_a, v_b, v_c, v_d, and v_e in Eqs. (41)–(43) are also well-defined material parameters, but to compensate for the approximations introduced into the MGPT, these latter quantities, together with the volume term $E_{\rm vol}$ in Eq. (40), are fit to a combination of experimental and first-principles DFT data on basic material properties. Specifically one fits, as a function of volume in the stable-solid bcc phase, a blend of experimental data at ambient pressure and DFT data at high pressure on the cold EOS, the shear elastic moduli C' and C_{44}, the unrelaxed vacancy formation energy $E^0_{\rm vac}$, and the Debye temperature $\Theta_{\rm D}$, subject to the additional constraint of the compressibility sum rule, which reduces the number of independent parameters from six to five. The calculated volume dependence of each of the d-band coefficients v_α is shown in Fig. 1(a) for the present case of Ta6.8x, where several technical improvements in the fitting scheme, as described below, have been introduced. From those results, one can see that the fundamental theoretical MGPT requirements [7], $v_b \gg v_a > 0$ and $v_e > v_d > 0$, are all well maintained.

Refinement of our basic MGPT fitting scheme has taken place over a number of generations of bcc transition-metal potentials [7–9,33], and the present Ta6.8x potentials represent a systematic numerical improvement over the previous Ta4 potentials [9,33] in three specific areas. First, a smoother blend of the input experimental and DFT data has been used through explicit analytic representations of that data, including (i) a universal-equation-of-state representation [34] of the cold EOS functions $E_0(\Omega)$ and $P_0(\Omega)$; (ii) power-series representations of $C'(P)$ and $C_{44}(P)$ in terms of pressure derivatives of the shear moduli; and (iii) explicit expression of the volume dependence of $\Theta_{\rm D}(\Omega)$ in terms of the measured Grüneisen parameter. While these analytic representations of the input data do improve the overall smoothness of the fitted parameters $E_{\rm vol}(\Omega)$ and $v_\alpha(\Omega)$, they do at the same time restrict the high-pressure limit of the $T = 0$ treatment to about 420 GPa in Ta6.8x, as compared to 1000 GPa in Ta4. The second area of improvement in Ta6.8x has been a more robust analytic fit to the hard-core potential $v_2^{\rm hc}(r,\Omega)$ in Eq. (41), allowing the full pair potential $v_2(r,\Omega)$ to be reliably extended to smaller separations, which are of direct interest in the high-temperature liquid.

Finally, these two general improvements combined have allowed the MGPT Ta6.8x potentials to be defined on a finer volume mesh, quantified by the reduced volume parameter $x = (\Omega/\Omega_0)^{1/3}$. Specifically, we have calculated the potentials on a uniform x mesh in increments of 0.01 over a range $0.80 \leqslant x \leqslant 1.08$, corresponding to 29 atomic volumes in all. Representative behavior of the Ta6.8x potentials is shown in Fig. 1(b) for the pair potential v_2, in Fig. 2(a) for the three-ion potential v_3, and in Fig. 2(b) for the four-ion potential v_4. Note that v_2 ranges from strongly attractive at large volume to completely repulsive at small volume, while v_3 is generally repulsive, but small in magnitude, and v_4 is significantly larger but necessarily oscillatory. Overall,

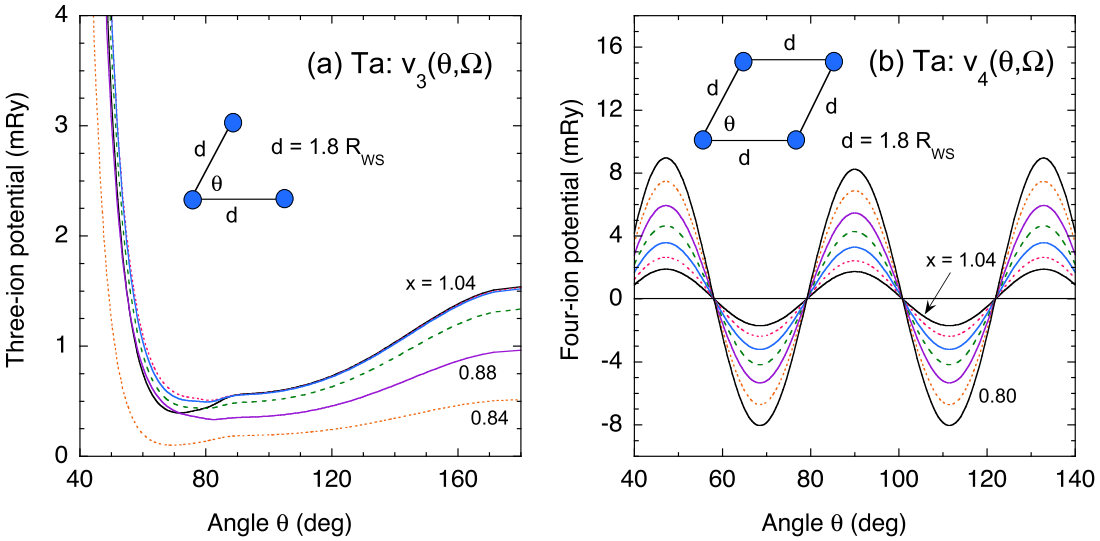

FIG. 2. (Color online) Angular and volume dependence of the Ta6.8x multi-ion MGPT potentials v_3 (a) and v_4 (b) for specific near-neighbor configurations at selected volumes, in x increments of 0.04 with $x = (\Omega/\Omega_0)^{1/3}$.

the numerical improvements in the Ta6.8x potentials lead to more accurate calculated thermodynamics from QHLD and from MGPT-MD simulations than is obtained with the Ta4 potentials.

B. QHLD, MD, and VPT implementation of MGPT potentials

In the present work, we have applied the Ta6.8x potentials in QHLD calculations and MGPT-MD simulations assuming a potential-energy function $U(\mathbf{R}) \equiv E_{\rm tot}(\mathbf{R},\Omega)$ in the ion equations of motion and using the advanced matrix representation of the MGPT total-energy functional [10], which provides maximum computational efficiency and accuracy. In this implementation, the angular functions L, P, and M in Eqs. (42) and (43) are evaluated on the fly during an MD simulation through d-state matrix multiplication, while the multi-ion forces that move the ions are determined analytically. All of the present MGPT-MD simulations have been performed in standard fixed-shape cubic computational cells at constant volume, using 250-ion ensembles for the bcc and liquid phases and 256-ion ensembles for the metastable-fcc phase. Constant simulation temperature has been maintained with a Gaussian thermostat [8,35–37]. The constant-volume MGPT-MD simulations have been performed along selected isochores at x increments of 0.04 between $x = 0.80$ and $x = 1.08$, corresponding to a direct treatment of 8 of the 29 volumes on the full x mesh. MD-derived thermodynamic data at intermediate volumes have been obtained by interpolation. The QHLD calculations of bcc quasiharmonic phonons and corresponding ion-thermal thermodynamic functions, on the other hand, have been performed directly on all 29 x-mesh volumes.

The volume-dependent effective pair potential $v_2^{\rm eff}$ that is required in VPT to obtain $\bar{z}$, the optimized reference potential $v_{\rm ref}(r,\bar{z})$, and the liquid reference free energy $A_{\rm ion}^{\rm ref}(\Omega,T_{\rm ref})$ for Eq. (21), is calculated numerically by averaging over the MGPT multi-ion potentials v_3 and v_4 in the liquid at temperature $T_{\rm ref}$:

$$v_2^{\rm eff}(R_{ij};\Omega) = v_2(R_{ij},\Omega) + \frac{1}{3}\left\langle {\sum_k}' v_3(ijk;\Omega)\right\rangle + \frac{1}{12}\left\langle {\sum_{k,l}}' v_4(ijkl;\Omega)\right\rangle. \quad (44)$$

In the present Ta applications, we have taken $T_{\rm ref} = 25\,000$ K. The behavior of $v_2^{\rm eff}$ is compared with both that of v_2 and that of the corresponding optimized r^{-12} reference potential $v_{\rm ref}$ in Fig. 3 at the volume $\Omega = \Omega_0$. Note that $v_{\rm ref}$ is a good match to $v_2^{\rm eff}$ in the short-range repulsive region important to

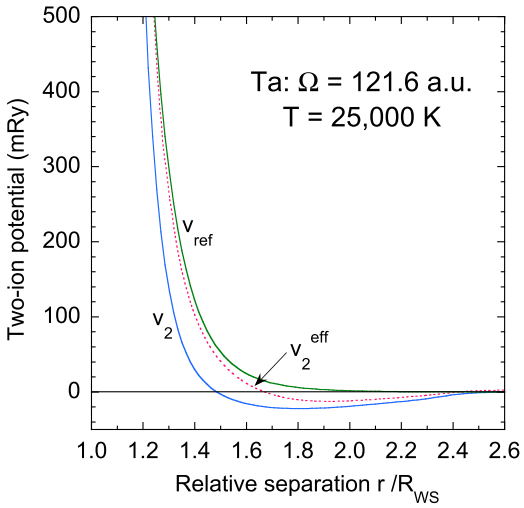

FIG. 3. (Color online) Effective pair potential $v_2^{\rm eff}$ in high-temperature liquid Ta at 25 000 K for $\Omega = \Omega_0$, as calculated from the present Ta 6.8x MGPT potentials v_2, v_3, and v_4 via Eq. (44) and as used to obtain an optimized r^{-12} reference potential $v_{\rm ref}$ for the same conditions.

the high-temperature liquid and that $v_2^{\rm eff}$ is everywhere more repulsive than v_2.

C. Stable-solid bcc free energy

In agreement with first-principles DFT calculations [16,38], Ta modeled with multi-ion MGPT potentials is both mechanically and thermodynamically stable in the bcc phase at $T = 0$ over the present pressure range, which extends up to 420 GPa at this temperature. Real quasiharmonic phonon frequencies are calculated throughout the Brillouin zone at all volumes within this pressure range. The quality of the MGPT phonons obtained with the Ta6.8x potentials was previously illustrated in Fig. 5 of Ref. [12], where calculated frequencies at the [100] and [110] zone boundaries were compared with DFT results [38] for a range of volumes and with experiment [39] at ambient conditions. As discussed in Ref. [12], there is good agreement among the MGPT, DFT, and experimental results, except for the anomalous transverse T_2[110] phonon frequency, which is underestimated with current MGPT Ta6.8x potentials.

Regarding MGPT calculation of the quasiharmonic component of the ion-thermal free energy, the Brillouin-zone sums in Eq. (16) for $A_{\rm ion}^{\rm qh}$ and Eq. (17) for $E_{\rm ph}^{0}$ have been carried out over 506 **q** points in the irreducible (1/48th) wedge of the bcc BZ at each of the 29 volumes on our fine volume mesh. The volume dependence, and corresponding pressure dependence, of the Debye temperature $\Theta_{\rm D}$ as calculated from Eqs. (17) and (19) with the present Ta6.8x potentials is shown in Fig. 4(a) and compared with the previous result [9] obtained from the Ta3 potentials (and as also obtained from the Ta4 potentials). In each case, $\Theta_{\rm D}(\Omega_0)$ has been constrained by experiment at ambient pressure through the measured phonon dispersion curves [39]. A similar comparison is made in Fig. 4(b) for the quasiharmonic ion-Grüneisen parameter $\gamma_{\rm ion}^{\rm qh}$, as calculated in the high-temperature limit, $T \gg \Theta_{\rm D}$, where one has $\gamma_{\rm ion}^{\rm qh}(\Omega) = \Omega P_{\rm ion}^{\rm qh}/E_{\rm ion}^{\rm qh}$, noting that $\gamma_{\rm ion}^{\rm qh}$ is effectively independent of temperature above $\Theta_{\rm D}$. While the improved Ta6.8x potentials and accompanying finer volume mesh have little quantitative effect on $\Theta_{\rm D}$, they do clearly impact derivative quantities like $\gamma_{\rm ion}^{\rm qh}$, especially at high pressure above 100 GPa. As also shown in Fig. 4(b), the measured Grüneisen parameter of 1.64 at ambient volume $\Omega = \Omega_0$ and room temperature [40] lies within about 3%, but halfway between, the Ta3-Ta4 and Ta6.8x quasiharmonic values of 1.69 and 1.59, respectively.

We also note in this regard that the volume or pressure dependence of the room temperature Grüneisen parameter, $\gamma(\Omega, T = 300\ {\rm K}) \cong \gamma_{\rm ion}^{\rm qh}(\Omega)$, is not quantitatively well constrained in bcc Ta by either theory or experiment. In particular, first-principles DFT calculations [15,41,42] yield a rather wide range of behavior for this quantity. Bercegeay and Bernard [41] calculated an ambient pressure value for $\gamma_{\rm ion}^{\rm qh}(\Omega_0)$ of about 1.53, in reasonable agreement with both experiment and Ta6.8x MGPT, but these authors found only a modest pressure dependence in $\gamma_{\rm ion}^{\rm qh}(\Omega)$, with a decline in value to about 1.3 at 400 GPa, which is about 20% *higher* than our present MGPT result at that pressure. In contrast, Cohen and Gülseren [42] and Taioli *et al.* [15] calculated relatively high values for room-temperature γ at ambient pressure of about 2.1 and 2.3, respectively, followed by rapid declines in value with increasing pressure. In these latter calculations, γ declined to about 1.0 at 275 and 200 GPa, respectively, which is 14% and 22% *lower* than the present MGPT results at these pressures.

The Cohen and Gülseren [42] and Taioli *et al.* [15] Grüneisen parameter calculations were done in the context of respective weak-coupling treatments of thermodynamic properties in bcc Ta, including consideration of the temperature dependence of such thermodynamic derivatives, a subject we will return to at the end of this section. In this regard, both Cohen and Gülseren [42] and Taioli *et al.* [15] added electron-thermal contributions to a quasiharmonic phonon contribution

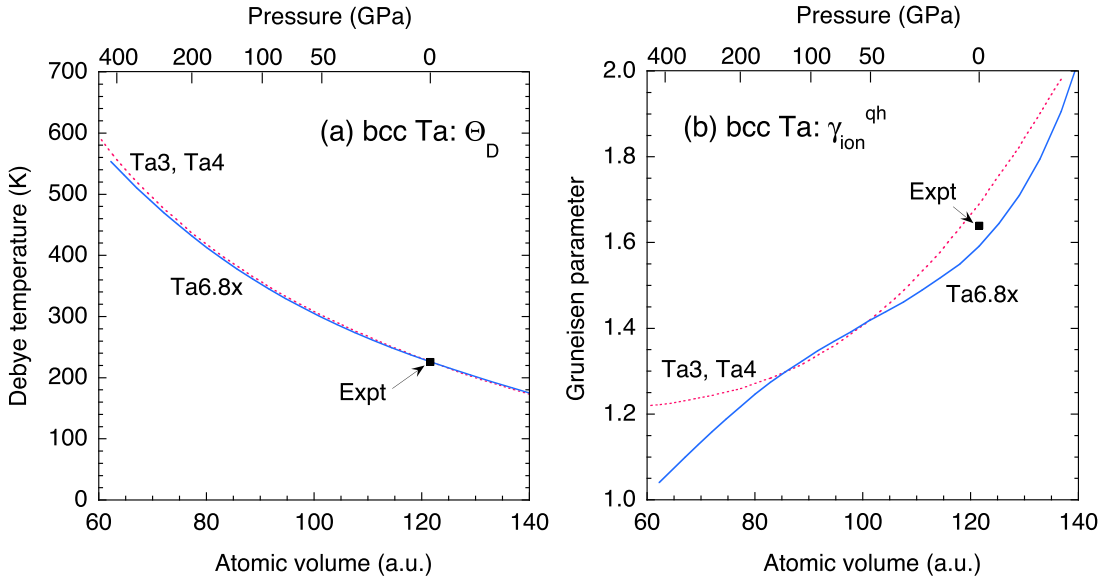

FIG. 4. (Color online) Volume and pressure dependence of the Debye temperature $\Theta_{\rm D}$ (a) and the quasiharmonic ion-Grüneisen parameter $\gamma_{\rm ion}^{\rm qh}$ (b) in bcc Ta, as calculated from the present MGPT Ta6.8x potentials, and as compared with corresponding results obtained from previous Ta3 [9] and Ta4 [9–11,33] potentials and from experiment at ambient conditions [39,40].

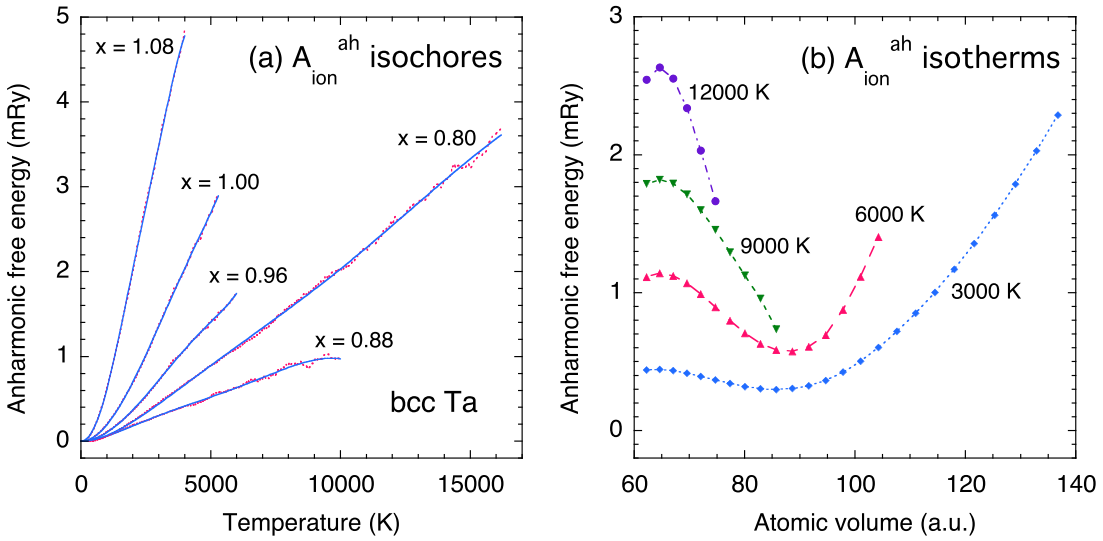

FIG. 5. (Color online) Anharmonic free energy in bcc Ta, as obtained from MGPT-RSMD simulations with the present Ta6.8x potentials. (a) Five selected isochores of the eight total calculated, with $x = (\Omega/\Omega_0)^{1/3}$. Shown are both the raw simulation data (short dashed lines) and smooth fits (solid lines) to the data via Eq. (45). (b) Four selected high-temperature isotherms obtained via interpolation on the eight fitted isochores and displayed for $T < T_{\rm L}(\Omega)$.

in their treatments, exactly as we do here, but Taioli *et al.* [15] neglected anharmonic effects entirely in calculating the temperature dependence of γ. Cohen and Gülseren [42], on the other hand, included anharmonic effects very approximately in their classical thermal EOS through a simple particle-in-cell model. In contrast to both of these treatments, we effectively include anharmonic effects without further approximation in applying our generalized RSMD method, as we now discuss for tantalum.

In stable-solid phases, it is generally a large computational challenge to obtain accurate anharmonic free energies, and this is particularly so in the present Ta example, where $A_{\rm ion}^{\rm ah}$ is small and only 1–5 mRy in magnitude near melt. Here we use this challenge to demonstrate both the power of RSMD simulation so applied and the utility of isolating anharmonic effects through Eq. (18). To obtain high convergence of $A_{\rm ion}^{\rm ah}$ to 0.1 mRy, which is needed to calculate smooth thermodynamic derivatives at high temperature, has required integrating over the temperature range from $x_{\rm D}\Theta_{\rm D}$ to $x_{\rm L}^{\rm max}T_{\rm L}$ very slowly, with 3×10^6 time steps at $x = 1.08$, increasing to 8×10^6 time steps for $x \leqslant 0.92$. We have so calculated $A_{\rm ion}^{\rm ah}$ along our eight simulation isochores ranging from $x = 0.80$ to $x = 1.08$, as illustrated in Fig. 5(a), with temperature-limit parameters $x_{\rm D} = 0.8$ and $x_{\rm L}^{\rm max} = 1$–2. As also demonstrated in Fig. 5(a), each simulated isochore can be smoothly fit with a polynomial expansion of the form

$$A_{\rm ion}^{\rm ah}(\Omega,T) = A_2T^2 + A_3T^3 + A_4T^4 + A_5T^5 + A_6T^6, \tag{45}$$

where the A_n are volume-dependent coefficients. The leading T^2 term in this expansion ensures the proper behavior of $A_{\rm ion}^{\rm ah}$ at low temperature and effectively corrects the small error incurred by starting the RSMD simulation at finite temperature. Taking into account Eqs. (9) and (15), and the general requirement of thermodynamic consistency, the corresponding anharmonic component of the total internal energy is then given by

$$E_{\rm ion}^{\rm ah}(\Omega,T) = -A_2T^2 - 2A_3T^3 - 3A_4T^4 - 4A_5T^5 - 5A_6T^6. \tag{46}$$

The smooth values of $A_{\rm ion}^{\rm ah}$ and $E_{\rm ion}^{\rm ah}$ so calculated on the eight isochores have then been extended to the full 29-volume mesh by numerical interpolation. Selected isotherms of $A_{\rm ion}^{\rm ah}$ on the full volume mesh are displayed in Fig. 5(b), and reveal that $A_{\rm ion}^{\rm ah}$ generally increases for Ta in both expansion and compression with a minimum occurring in the 80–100 a.u. volume range. Finally, values of the anharmonic pressure, $P_{\rm ion}^{\rm ah} = -\partial A_{\rm ion}^{\rm ah}/\partial\Omega$, have been calculated by direct numerical differentiation on the full volume mesh.

An independent check on the numerical accuracy of $E_{\rm ion}^{\rm ah}$ obtained from Eq. (46) can be made as follows. If one performs a standard MD simulation at constant volume and temperature, $E_{\rm ion}^{\rm ah}$ can be extracted from the total simulated ion-thermal energy $E_{\rm ion}^{\rm sol}$ as $E_{\rm ion}^{\rm ah} = E_{\rm ion}^{\rm sol} - 3k_{\rm B}T$. From a well equilibrated MGPT-MD simulation near melt conditions of $\Omega = \Omega_0$ and $T = 4000$ K, we thereby have obtained $E_{\rm ion}^{\rm ah} = -0.6 \pm 0.2$ mRy, where the statistics on $E_{\rm ion}^{\rm sol}$ have been accumulated for 10 ps. This result agrees with the corresponding value of $E_{\rm ion}^{\rm ah} = -0.6 \pm 0.1$ mRy calculated from Eq. (46) for the same volume and temperature.

With a bcc cold energy $E_0 = E_0^{\rm bcc}$, the total free energy of the stable solid,

$$\begin{aligned} A_{\rm bcc}(\Omega,T) &= E_0^{\rm bcc}(\Omega) + A_{\rm ion}^{\rm bcc}(\Omega,T) + A_{\rm el}(\Omega,T) \\ &= E_0^{\rm bcc}(\Omega) + A_{\rm ion}^{\rm qh}(\Omega,T) \\ &\quad + A_{\rm ion}^{\rm ah}(\Omega,T) + A_{\rm el}(\Omega,T), \end{aligned} \tag{47}$$

has then been calculated for bcc Ta on the full volume mesh from its component parts. Corresponding results also have been obtained for the total internal energy $E_{\rm bcc}$ and total pressure $P_{\rm bcc}$, completing the full bcc equation of state. A sensitive check on the physical accuracy of the thermal components of $A_{\rm bcc}$ and $E_{\rm bcc}$ can be made in terms of measured

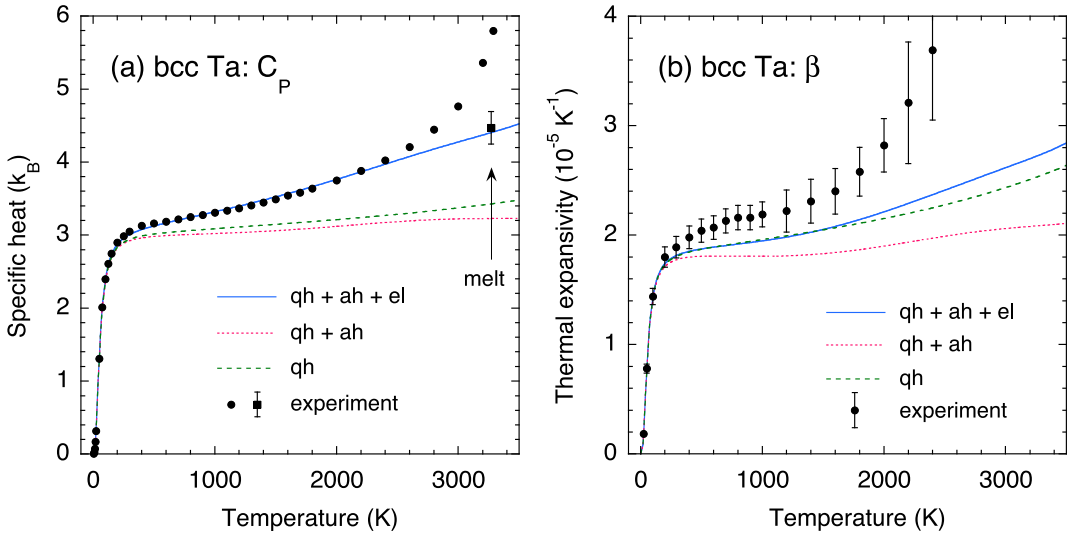

FIG. 6. (Color online) Thermodynamic derivatives in bcc Ta at zero pressure, as calculated in the quasiharmonic (qh), quasiharmonic plus anharmonic (qh + ah), and quasiharmonic plus anharmonic plus electron-thermal (qh + ah + el) limits of the present theory, and as compared to experiment. (a) Constant-pressure specific heat C_P, with the measured data from Ref. [43] (solid circles) and Refs. [44–46] (solid square). (b) Thermal expansion coefficient or expansivity β, with the measured data from Ref. [47] (solid circles).

thermodynamic derivatives, namely, the temperature dependence of the constant-pressure specific heat C_P and of the thermal expansion coefficient or expansivity $\beta = \Omega^{-1}(\partial\Omega/\partial T)_P$ at ambient pressure. We compare our calculated results for these quantities in three theoretical limits against experimental data [43–47] in Fig. 6. The limits so treated are first the full theory, with complete quasiharmonic, anharmonic, and electron-thermal contributions; second, the quasiharmonic plus anharmonic limit, with electron-thermal contributions omitted ($A_{el} = 0$); and third, the quasiharmonic limit, with both anharmonic and electron-thermal contributions omitted ($A_{el} = A_{ion}^{ah} = 0$).

Regarding the specific heat C_P in Fig. 6(a), the full theory is in close agreement with the experimental data of Hultgren *et al.* [43] up to about 2600 K, capturing the observed behavior in both the low-temperature quantum Bose-Einstein regime below 300 K and the classical Boltzmann regime above that point. The anharmonic contribution to this result is seen to be very small, while the much larger electron-thermal contribution is clearly essential to the quantitative agreement above room temperature. The observed steep rise in C_P above 2600 K in the Hultgren *et al.* data is not predicted by the present theory, but this feature is well known to be sensitive to impurities and other experimental factors, so this shortcoming is not necessarily significant. In this regard, the high-temperature behavior of C_P that we have calculated above 2600 K is in qualitative agreement with the corresponding DFT-based result of Cohen and Gülseren [42]. In addition, and as also shown in Fig. 6(a), the present full theory result for C_P at melt is in good agreement with the value derived from isobaric expansion measurements [44–46].

Regarding the thermal expansion coefficient β in Fig. 6(b), the present full-theory result is in good accord with the measured data of Touloukian *et al.* [47] up to about 400 K and still in reasonable agreement to 1000 K, again capturing the observed behavior in both the quantum and classical temperature regimes. Above 1000 K, however, the data has large error bars and begins to diverge from the theory, and only provisional values of thermal expansion were measured above 2000 K. In a similar manner, the steep rise in the Touloukian *et al.* data above 2000 K was found to move rapidly above the corresponding DFT-based result of Cohen and Gülseren [42] as well as the EAM-MD calculations of β in Ta by Strachan *et al.* [48].

Finally, we return to consideration of the temperature dependence of the Grüneisen parameter $\gamma(\Omega, T)$. In its general form, this quantity is the thermodynamic derivative

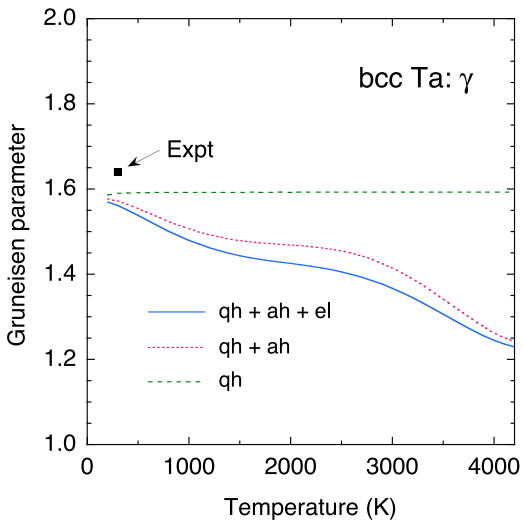

FIG. 7. (Color online) Temperature dependence of the Grüneisen parameter $\gamma(\Omega_0, T)$ in bcc Ta at ambient volume, as calculated in the quasiharmonic (qh), quasiharmonic plus anharmonic (qh + ah), and quasiharmonic plus anharmonic plus electron-thermal (qh + ah + el) limits of the present theory, and as compared to experiment at room temperature [40].

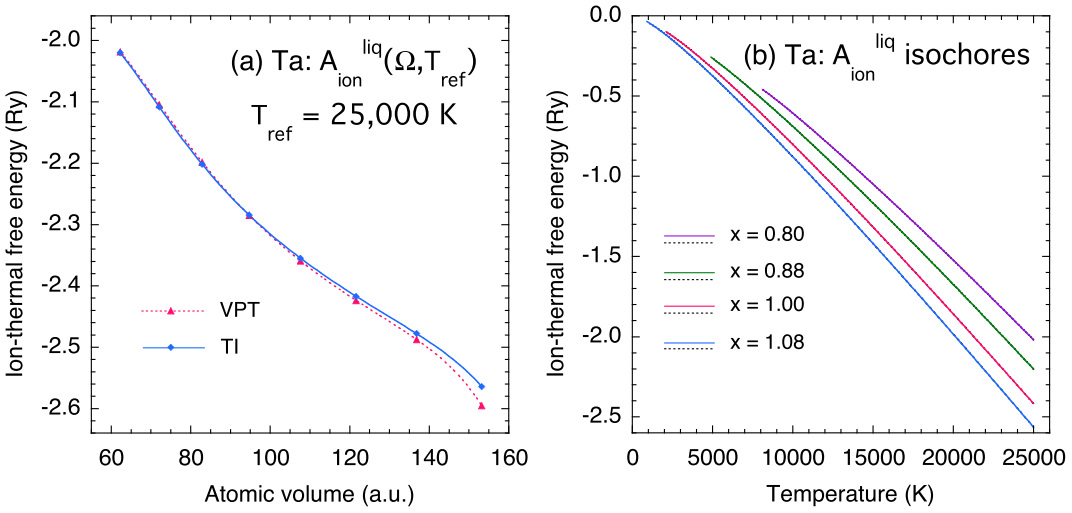

FIG. 8. (Color online) Ion-thermal free energy $A_{\rm ion}^{\rm liq}$ in liquid Ta, as obtained with the present Ta6.8x MGPT potentials. (a) Reference isotherm $A_{\rm ion}^{\rm liq}(\Omega,T_{\rm ref})$ for $T_{\rm ref}=25\,000$ K, as calculated both approximately from variational perturbation theory (VPT), using Eq. (30), and more accurately from thermodynamic integration (TI), using Eq. (21). (b) Four selected isochores of the eight total calculated via MGPT-RSMD simulation, in x increments of 0.08 with $x=(\Omega/\Omega_0)^{1/3}$. Shown are both the raw simulation data (short dashed lines) and smooth fits (solid lines) to the data using Eq. (48).

$\gamma=\Omega(\partial P/\partial E)_\Omega=\Omega\beta B_T/C_\Omega$, where B_T is the isothermal bulk modulus and C_Ω is the constant volume specific heat. In Fig. 7 we plot our calculated results for $\gamma(\Omega,T)$ as a function of temperature from 200 to 4200 K at ambient volume, $\Omega=\Omega_0$, in the same three theoretical limits considered above for $C_{\rm P}$ and β. As expected, $\gamma(\Omega_0,T)$ calculated in the quasiharmonic limit is essentially independent of temperature above the Debye temperature of 226 K at ambient volume. At the same time, the anharmonic free-energy contribution to γ produces a significant temperature dependence to this quantity above room temperature, with the Grüneisen parameter monotonically reduced in value above 300 K. A qualitatively similar but much smaller contribution comes from the electron-thermal component. Our full-theory value of $\gamma(\Omega_0,T)$, with quasiharmonic, anharmonic and electron-thermal contributions, is thereby lowered by 22% from a value of 1.59 at 300 K to 1.24 at 4000 K. The same decrease in the value of γ by 0.35 between 300 and 4000 K was calculated by Cohen and Gülseren at ambient pressure [42]. In contrast, Taioli *et al.* [15] calculated a much larger decrease of about 0.60 for the same conditions, even though they did not include any account of anharmonic effects in their treatment. Even more puzzling, most of the latter drop occurred at temperatures below 1000 K, which does not seem physically realistic.

D. Liquid free energy

In the liquid, the biggest computational challenge is to calculate an accurate reference ion-thermal free energy $A_{\rm ion}^{\rm liq}(\Omega,T_{\rm ref})$ along a high-temperature isotherm. In the case of Ta we have successfully applied the combined VPT and TI methodology described above in Sec. II C to that task at a reference temperature $T_{\rm ref}=25\,000$ K, with a choice of a bcc cold energy $E_0(\Omega)=E_0^{\rm bcc}(\Omega)$. Using variational perturbation theory, upper and lower bounds to the free energy and an averaged variational parameter $\bar{z}(\Omega)$ were established at each of the eight volumes on our simulation mesh. Using thermodynamic integration from an r^{-12} reference system, optimized at each volume using $\bar{z}$, to the true system, $A_{\rm ion}^{\rm liq}(\Omega,T_{\rm ref})$ was then calculated on the simulation mesh from Eq. (21). At each volume, only five points in the integral contained in Eq. (21) were necessary to obtain $A_{\rm ion}^{\rm liq}(\Omega,T_{\rm ref})$ to sub-mRy numerical accuracy. Our final result for $A_{\rm ion}^{\rm liq}(\Omega,T_{\rm ref})$ is plotted in Fig. 8(a) and compared with the approximate baseline VPT value of this quantity as calculated from Eq. (30), which overestimates $A_{\rm ion}^{\rm liq}(\Omega,T_{\rm ref})$ by 2 mRy or less at small volumes, but underestimates this quantity by as much as 31 mRy at large volumes.

With $A_{\rm ion}^{\rm liq}(\Omega,T_{\rm ref})$ thereby established, MGPT-RSMD simulations of $A_{\rm ion}^{\rm liq}(\Omega,T)$ were then performed downward in temperature from $T_{\rm ref}$ to $0.5T_{\rm L}(\Omega)$ along the eight simulation isochores. Raw simulation data for $A_{\rm ion}^{\rm liq}(\Omega,T)$ together with smooth analytic fits to the data are shown in Fig. 8(b) for four selected isochores. The MGPT-RSMD simulation results were obtained with 2×10^6 time steps at all volumes and were found to be well converged. Similar good results were also obtained with as few as 5×10^5 time steps, and increases first to 1×10^6 time steps and then to 2×10^6 time steps produced little change in the results.

The analytic fits of the ion-thermal free-energy data shown in Fig. 8(b) were obtained using the form

$$\begin{aligned}A_{\rm ion}^{\rm liq}(\Omega,T)=&\,C_0\tau-C_1\tau\,\ln\,\tau+C_2\tau(\tau-1)\\&+C_3\tau(\tau^2-1)+C_4\tau(\tau^3-1)\\&+C_5\tau(\tau^4-1)+C_6\tau(\tau^5-1),\end{aligned}\qquad(48)$$

where $\tau=T/T_{\rm ref}$ and where the C_n are volume-dependent coefficients that include the constraint $C_0(\Omega)=A_{\rm ion}^{\rm liq}(\Omega,T_{\rm ref})$. Consistent with Eq. (9), the corresponding ion-thermal

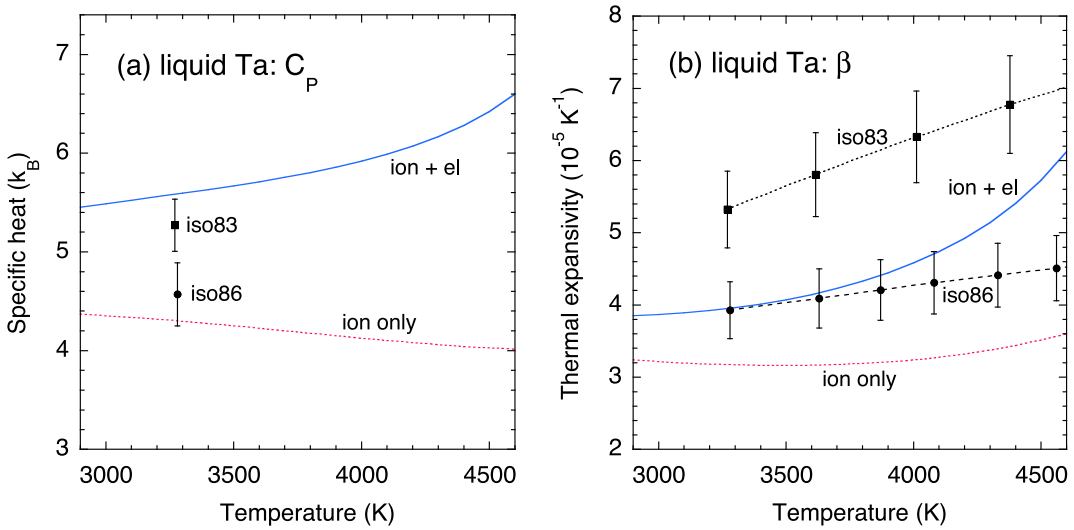

FIG. 9. (Color online) Thermodynamic derivatives in liquid Ta at zero pressure, as calculated both without electron-thermal contributions (ion only) and with electron-thermal contributions (ion + el) in the present theory, and as compared to experimental isobaric expansion data from Ref. [45] (iso83) and Ref. [46] (iso86). (a) Constant-pressure specific heat C_P, with the measured data at melt. (b) Thermal expansion coefficient or expansivity β.

component of the total internal energy is given by

$$E_{\rm ion}^{\rm liq}(\Omega,T) = C_1\tau - C_2\tau^2 - 2C_3\tau^3 - 3C_4\tau^4 - 4C_5\tau^5 - 5C_6\tau^6, \quad (49)$$

which is then analogous to Eq. (45) for $A_{\rm ion}^{\rm ah}$ except for the necessary addition of a term linear in the temperature. While Eqs. (48) and (49) can be used directly in this form, with six independent fitting parameters at each volume, in practice it is more desirable to introduce an additional constraint on $E_{\rm ion}^{\rm liq}$ at the reference temperature:

$$E_{\rm ion}^{\rm liq}(\Omega,T_{\rm ref}) = C_1 - C_2 - 2C_3 - 3C_4 - 4C_5 - 5C_6. \quad (50)$$

Here we have calculated accurate values of $E_{\rm ion}^{\rm liq}(\Omega,T_{\rm ref})$ for Ta at the eight volumes on our simulation mesh with independent MGPT-MD simulations. Combining Eq. (50) with Eqs. (48) and (49) not only ensures that both $A_{\rm ion}^{\rm liq}$ and $E_{\rm ion}^{\rm liq}$ are accurately maintained along the $T = T_{\rm ref}$ isotherm, but it produces a very robust fit of $A_{\rm ion}^{\rm liq}$ along all eight MGPT-RSMD isochores in liquid Ta, as illustrated in Fig. 8(b). The values of $A_{\rm ion}^{\rm liq}$ and $E_{\rm ion}^{\rm liq}$ so calculated have been extended to the full 29-volume mesh by numerical interpolation. Values of the ion-thermal pressure, $P_{\rm ion}^{\rm liq} = -\partial A_{\rm ion}^{\rm liq}/\partial\Omega$, have then been calculated by direct numerical differentiation on the full volume mesh.

The total free energy of the liquid,

$$A_{\rm liq}(\Omega,T) = E_0^{\rm bcc}(\Omega) + A_{\rm ion}^{\rm liq}(\Omega,T) + A_{\rm el}(\Omega,T), \quad (51)$$

has been calculated for Ta on the full volume mesh from its three component parts, together with corresponding results obtained for the total internal energy $E_{\rm liq}$ and total pressure $P_{\rm liq}$. As for the bcc solid, a sensitive physical check on the thermal components of $A_{\rm liq}$ and $E_{\rm liq}$ can be made in terms of the temperature dependence of the thermodynamic derivatives C_P and β at ambient pressure. We display our calculated values of C_P and β for liquid Ta in Figs. 9(a) and 9(b), respectively, as obtained both from the full theory, with ion- and electron-thermal components, and in the ion-thermal only limit ($A_{\rm el} = 0$). As expected, the inclusion of the electron-thermal component has a big impact on the calculated derivatives, and our results in the liquid are very consistent with those obtained in the bcc solid (Fig. 6). With electron-thermal effects included, we find that C_P at melt rises from $4.4k_B$ in the bcc solid to $5.6k_B$ in the liquid, which is in good agreement with the temperature-corrected isobaric data of Shaner *et al.* [44] as reported by Gathers [45]. On the other hand, Berthault *et al.* [46] find a much smaller rise of C_P to only $4.6k_B$ in the liquid in their isobaric measurements. Similarly, with the full theory we find that β at melt rises from 2.7×10^{-5} K^{-1} in the bcc solid to 4.0×10^{-5} K^{-1} in the liquid. In this case, the liquid result at melt is in close agreement with the Berthault *et al.* [46] data, but 20% less than inferred from Gathers [45].

E. Melt curve and equation of state

Using the detailed computational methodology discussed above in Secs. III C and III D, full-range EOS tables for the bcc and liquid phases of Ta have been assembled. These tables include the total pressure P, the total internal energy E, and the total free energy A evaluated as a function of volume and temperature on the full 29-volume mesh and at temperature intervals of 100 K up to 25 000 K. In this section, we use these results to examine the equilibrium melt curve connecting the bcc-solid and liquid EOS surfaces, as well as basic pressure-volume compression curves, namely, the 300-K isotherm and the principal shock Hugoniot, which can be directly compared to experiment.

The melt curve has been calculated here using the standard Helmholtz free-energy construction, obtaining melt temperatures T_m as a function of pressure in 100 K intervals up to melt pressures P_m approaching 500 GPa. To examine melt sensitivities in Ta, we have calculated the melt curve not only with the full theory that we have developed, but also in the limit of no electron-thermal contributions ($A_{\rm el} = 0$) and

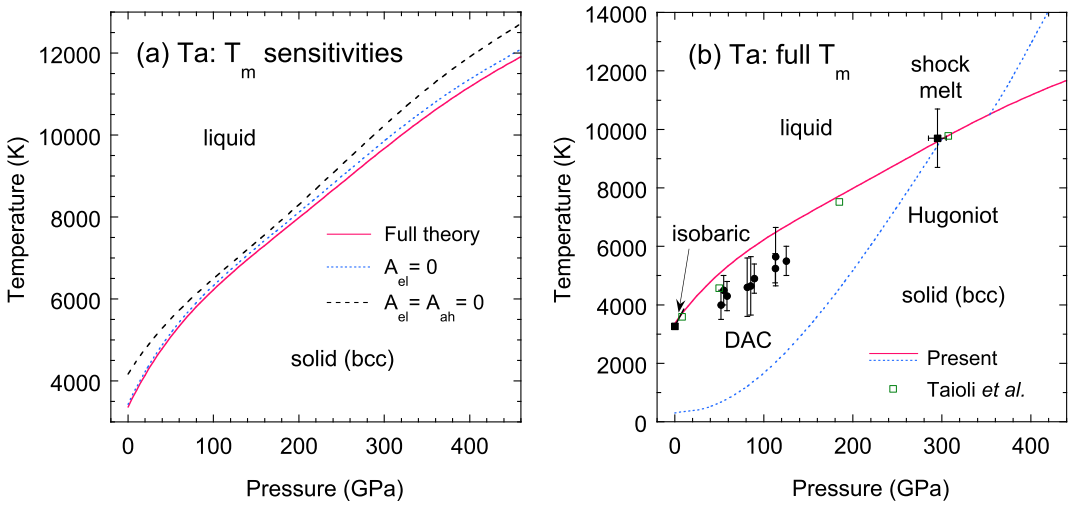

FIG. 10. (Color online) High-pressure melting in Ta, as calculated from the present bcc-solid and liquid free energies. (a) Sensitivity of the melt curve to electron-thermal (A_{el}) and anharmonic (A_{ah}) free-energy contributions. (b) Full-theory melt curve and principal Hugoniot, with comparison to experimental isobaric [44,45], DAC [49], and shock [50,51] melt data, and to the calculated first-principles melt points of Taioli *et al.* [15].

in the limit of both no electron-thermal and no anharmonic contributions ($A_{el} = A_{ah} = 0$). The three Ta melt curves so obtained are compared in Fig. 10(a). As expected, the effect of electron-thermal contributions is found to be small, lowering the melt curve by only 75–200 K, or less than 3%, across the entire pressure range considered. At the same time, and as previously discussed in Ref. [12], the bcc free-energy melt curve calculated in the $A_{el} = 0$ limit is in very good agreement with the corresponding result obtained in two-phase MGPT-MD melt simulations, thus validating the computational accuracy of our melt calculation in this limit. As also demonstrated in Fig. 10(a), the effect of anharmonic contributions on the Ta melt curve is considerably larger, especially at low pressures below 100 GPa, where T_m is lowered by up to 725 K or over 20%, and at very high pressures above 250 GPa, where T_m is lowered by up to 550 K. This finding is consistent with the fact that the anharmonic free energy in the bcc solid is generally calculated to be minimum at intermediate volumes and pressures, as was shown above in Fig. 5.

Our full-theory melt curve for Ta is compared with static and dynamic experimental data in Fig. 10(b). The calculated zero-pressure melt temperature of $T_m = 3349$ K and melt-curve slope of $dT_m/dP_m = 52.2$ K/GPa compare well with the values of 3270 K and 58.8 K/GPa, respectively, obtained from isobaric data [44,45]. At intermediate pressures, the recent static diamond-anvil-cell (DAC) data of Dewaele *et al.* in Ta [49], obtained in the pressure range 52–113 GPa, lie below our calculated melt curve, but these data also have large

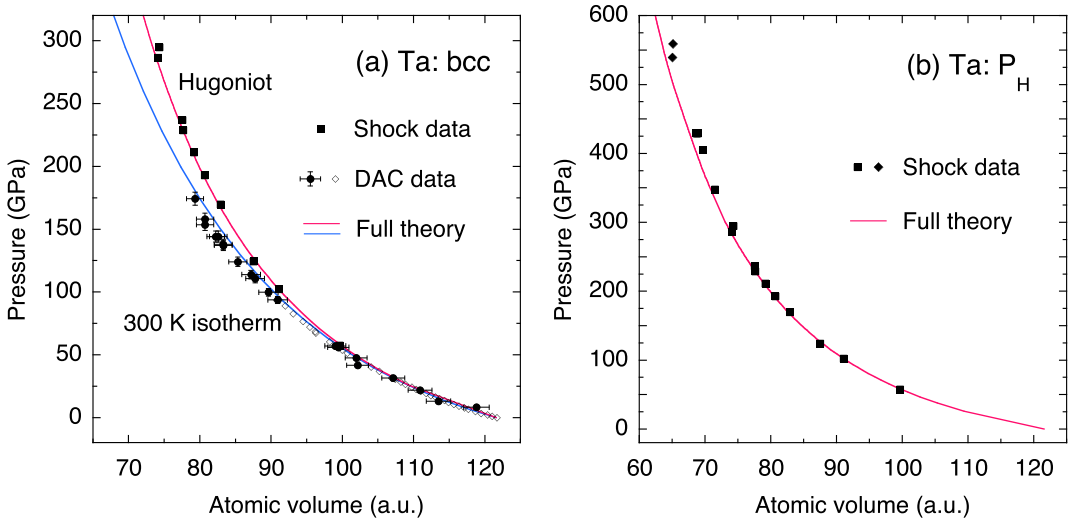

FIG. 11. (Color online) High-pressure EOS properties in Ta, as obtained from the present bcc and liquid equations of state and compared to experiment. (a) Room-temperature (300 K) isotherm and principal Hugoniot calculated in the bcc phase (solid lines), and compared, respectively, to static DAC data (solid circles from Ref. [52] and open diamonds from Ref. [53]) and dynamic shock data (solid squares from Ref. [54]). (b) Principal Hugoniot calculated in both the bcc solid and the liquid, and compared to shock data (solid squares from Ref. [54] and solid diamonds from Ref. [55]).

temperature errors bars of 500–1000 K. At high pressure, the intersection of the present calculated principal Hugoniot in the bcc solid with the melt curve is in excellent agreement with the measured onset of shock melting [50,51] at 295 GPa and 9700 K.

Also in Fig. 10(b), our full-theory melt curve for Ta is compared with the calculated first-principles melt results of Taioli *et al.* [15], which were obtained from a DFT-based TPT method [5]. Unlike their calculation of the Grüneisen parameter discussed above, the latter TPT method used by Taioli *et al.* [15] implicitly included anharmonic effects in the bcc solid. Thus the close agreement of our full-theory melt curve with the Taioli *et al.* [15] melt points shown in Fig. 10(b) is significant, as well as satisfying.

Our corresponding full-theory pressure-volume relations for the room-temperature (300-K) isotherm and principal Hugoniot are plotted in Fig. 11 and compared against static and dynamic experimental data. Figure 11(a) displays the results for these quantities in the bcc solid below about 300 GPa. Our calculated 300-K isotherm is in good agreement with the DAC data of Cynn and Yoo [52], measured to 174 GPa, and with the DAC data of Dewaele *et al.* [53], measured to 94 GPa. Similarly, our calculated bcc Hugoniot, whose temperature ranges from 300 to about 10 000 K, is in good agreement with the shock data on Mitchell and Nellis [54]. Figure 11(b) displays our calculated Hugoniot in both the bcc solid and the liquid, extending to 600 GPa. Reasonably good agreement with shock data [54,55] is maintained in the liquid as well, although above 400 GPa the calculated Hugoniot pressure is slightly underestimated. Also note that, as expected and in contrast to the calculated temperature-pressure Hugoniot [Fig. 10(b)], melting produces no visible discontinuity in the pressure-volume Hugoniot.

F. Metastable-fcc free energy

We finally turn to the case of calculating the free energy for a metastable phase, using the fcc phase of Ta as a prototype example. Fcc is one of a number of structures in Ta that is predicted to be mechanically unstable at $T = 0$, with calculated imaginary quasiharmonic phonon frequencies, but that is stabilized at high temperature and pressure by large anharmonic effects [12,16]. In particular, previous MGPT-MD simulations with Ta6.8x potentials [12] have shown that fcc Ta displays good mechanical stability near melt, yet remains thermodynamically less stable than bcc Ta, with a melt temperature that lies everywhere below that of bcc. Large-cell two-phase MGPT-MD simulations with 74 088 atoms were used in Ref. [12] to calculate a smooth fcc melt curve to 440 GPa in the $A_{\rm el} = 0$ limit. In the process, accurate data were obtained on the melt temperature $T_{\rm m}^{\rm fcc}$, melt pressure $P_{\rm m}^{\rm fcc}$, and solidus volume $\Omega_{\rm sol}^{\rm fcc}$, data that we have used here to establish a reference free energy for the fcc phase. Toward this end, we have carefully fit the fcc melt data so obtained in the analytic forms

$$T_{\rm m}^{\rm fcc}(x) = (3.6661 - 9.8710x + 9.0306x^2 - 2.7966x^3) \times 10^5 \text{ K} \quad (52)$$

and

$$P_{\rm m}^{\rm fcc}(x) = (2.8619 - 8.1213x + 7.7248x^2 - 2.4643x^3) \times 10^4 \text{ GPa}, \quad (53)$$

where $x = (\Omega_{\rm sol}^{\rm fcc}/\Omega_0)^{1/3}$ within the restricted range $1.04 \leqslant x \leqslant 0.80$. Combining the use of Eqs. (52) and (53) with interpolation on the $A_{\rm el} = 0$ liquid equation of state for Ta, we have calculated the fcc ion-thermal free energy $A_{\rm ion}^{\rm fcc}(\Omega, T_{\rm m}^{\rm fcc})$ along the melt curve using Eqs. (34) and (35), with a cold energy $E_0^{\rm fcc}(\Omega)$ for the fcc structure. Because the fcc melt curve lies significantly lower in temperature than the bcc melt curve, the accuracy of this procedure was improved by constructing a special liquid free energy and EOS in which the MGPT-RSMD simulations for the liquid were taken to lower temperature. Specifically, the liquid simulations for this purpose were performed downward in temperature from 25 000 to 1000 K, instead of down to $0.5T_{\rm L}$ as in Sec. III D above. These calculations were carried out along the eight simulation isochores, using 1×10^6 time steps in each case, with extension to the full 29-volume mesh by interpolation.

To obtain fcc ion-thermal free energies above and below the reference temperature $T_{\rm ref} = T_{\rm m}^{\rm fcc}$, we have used the reference free energy $A_{\rm ion}^{\rm fcc}(\Omega, T_{\rm m}^{\rm fcc})$ in Eq. (14) and performed MGPT-RSMD simulations to higher and lower temperature along the seven simulation isochores contained within the restricted volume range of Eqs. (52) and (53), using a total of 1×10^6 time steps in each case. The simulations to higher temperature were carried out from $T_{\rm m}^{\rm fcc}$ to $T_{\rm max}^{\rm fcc} = 17\,500$ K, while those to lower temperature were performed from $T_{\rm m}^{\rm fcc}$ to $0.5T_{\rm m}^{\rm fcc}$ K, which we estimate to be an approximate lower bound in temperature for the mechanical stability of the fcc structure. The fcc ion-thermal free-energy data so obtained were then fit with an analytic form analogous to Eq. (48) for the liquid:

$$A_{\rm ion}^{\rm fcc}(\Omega, T) = B_0\tau - B_1\tau \ln \tau + B_2\tau(\tau - 1) + B_3\tau(\tau^2 - 1) + B_4\tau(\tau^3 - 1) + B_5\tau(\tau^4 - 1) + B_6\tau(\tau^5 - 1), \quad (54)$$

where $\tau = T/T_{\rm max}^{\rm fcc}$, the B_n are volume-dependent coefficients, and $B_0(\Omega) = A_{\rm ion}^{\rm fcc}(\Omega, T_{\rm max}^{\rm fcc})$. From thermodynamic consistency, the corresponding ion-thermal component of the total fcc internal energy is given by

$$E_{\rm ion}^{\rm fcc}(\Omega, T) = B_1\tau - B_2\tau^2 - 2B_3\tau^3 - 3B_4\tau^4 - 4B_5\tau^5 - 5B_6\tau^6. \quad (55)$$

The values of $A_{\rm ion}^{\rm fcc}$ and $E_{\rm ion}^{\rm fcc}$ so calculated have then been extended to a fine 25-volume mesh by numerical interpolation. The fcc ion-thermal pressure, $P_{\rm ion}^{\rm fcc} = -\partial A_{\rm ion}^{\rm fcc}/\partial\Omega$, has been calculated by direct numerical differentiation on the fine volume mesh.

To test the numerical accuracy and self-consistency of our calculation of $A_{\rm ion}^{\rm fcc}(\Omega, T)$, the total fcc free energy in the $A_{\rm el} = 0$ limit was obtained by adding the cold energy $E_0^{\rm fcc}(\Omega)$ and assembling an fcc EOS table in the 2000–17 500 K temperature range. This result was then used together with the corresponding liquid free energy and EOS discussed above to perform a Helmholtz free-energy calculation of the fcc melt curve. The free-energy melt curve so calculated is compared

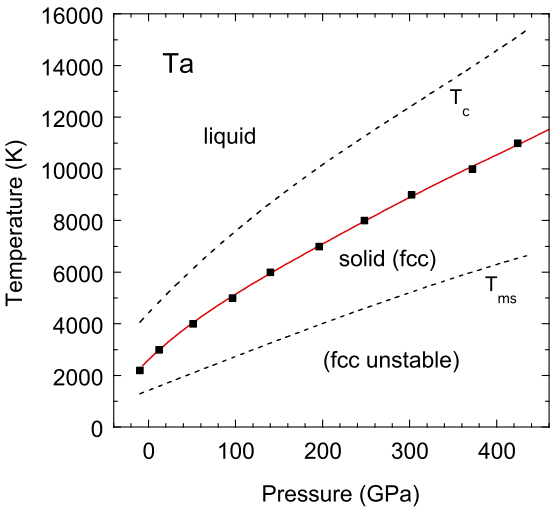

FIG. 12. (Color online) High-pressure melt curve for the metastable-fcc structure in Ta, as calculated without electron-thermal free energy contributions ($A_{\rm el} = 0$). Solid square points denote input melt data from two-phase MGPT-MD simulations [12], while the solid line is the calculated melt curve from the output fcc free energy and the liquid free energy. The dashed lines represent approximate upper ($T_{\rm c}$) and lower ($T_{\rm ms}$) bounds on fcc mechanical stability.

with the input two-phase melt data in Fig. 12. The agreement is seen to be excellent. We have also performed additional MGPT-MD simulations to determine actual approximate upper and lower temperature bounds on fcc mechanical stability, and these are plotted as a function of pressure in Fig. 12. To estimate the upper bound, we have calculated the critical temperature $T_{\rm c}$ to homogeneously melt the fcc solid at constant volume. To estimate the lower bound, we have observed from above the temperature $T_{\rm ms}$ at which the fcc lattice loses structural stability and begins to transform to another structure at constant volume. We find that $T_{\rm ms} \sim 0.5T_{\rm m}^{\rm fcc}$ is consistent with our choice of $0.5T_{\rm m}^{\rm fcc}$ as the lower temperature limit in the MGPT-RSMD simulations to determine fcc ion-thermal free energy.

As a final step, we have added the electron-thermal contribution $A_{\rm el}$ to form the total fcc free energy $A_{\rm fcc}$ at the same level of approximation as obtained above for the bcc structure in Sec. III C and for the liquid in Sec. III D:

$$A_{\rm fcc}(\Omega,T) = E_0^{\rm fcc}(\Omega) + A_{\rm ion}^{\rm fcc}(\Omega,T) + A_{\rm el}(\Omega,T). \qquad (56)$$

A corresponding total fcc EOS table was then assembled and the fcc free-energy melt calculation repeated. As expected, the impact of $A_{\rm el}$ on the fcc melt curve was found to be small, lowering the calculated melt temperature by 3% or less at all pressures, exactly as was the case for the bcc melt curve [Fig. 10(a)].

IV. CONCLUSIONS

In the present paper we have elaborated and implemented an efficient generalized RSMD method to calculate accurate Helmholtz free energies of weak-coupling materials characterized by temperature-independent ion forces and additive cold, ion-thermal, and electron-thermal free-energy components. With our method such materials can be treated in stable-solid phases, in the liquid, and in metastable phases alike over wide ranges of volume and temperature, with both significant cost savings and controllable numerical accuracy achieved in the central ion-thermal RSMD simulations. In stable-solid phases, our approach smoothly combines a QHLD calculation of the ion-thermal free energy at low temperatures with an accurate and isolated RSMD simulation of the anharmonic vibrational free-energy component at high temperatures to produce a seamless ion-thermal free energy from $T = 0$ to above melt at each volume of interest. In the liquid, we first use VPT to optimize an appropriate r^{-12} reference pair potential and then perform a smooth thermodynamic integration to the true system to establish an accurate reference free energy along a high-temperature isotherm at the top of the temperature range of interest. At each volume, a single RSMD simulation is then used to obtain an ion-thermal free energy for the liquid from the reference temperature down to below melt. In metastable solid phases, a reference free energy is established along the solidus melt line by using melt input from independent two-phase MD simulations combined with the calculated liquid free energy. For each volume, an RSMD simulation to higher temperature and an RSMD simulation to lower temperature are used to calculate the ion-thermal free energy within the limits of mechanical stability of the metastable phase.

We have specifically adapted our free-energy method to metals where the ion forces are well described by multi-ion MGPT interatomic potentials, together with the inclusion of small additional electron-thermal contributions to the free energy. Using refined Ta6.8x MGPT potentials in the QHLD, VPT, and RSMD calculations, we have successfully applied this method to the stable-bcc, liquid, and metastable-fcc phases of tantalum. For each phase, we have calculated a total Helmholtz free energy and its components to very high and unprecedented sub-mRy numerical accuracy over an extended volume range from up to 26% expansion to nearly twofold compression and temperatures up to 25 000 K. The small anharmonic vibrational free-energy component in the bcc solid, which is only 1–5 mRy in magnitude near melt in Ta, has been everywhere converged to 0.1 mRy. The physical accuracy of the total free energy obtained for each phase has been tested through the calculation of sensitive thermodynamic properties of Ta, including the specific heat and thermal expansivity in the bcc solid and the liquid at ambient pressure, the bcc and metastable-fcc melting curves to high pressure above 400 GPa, and the equation of state and shock Hugoniot in the bcc and liquid phases, extending to pressures of 600 GPa. In the process, we have also gained new insight into the roles of anharmonic and electron-thermal free-energy components on such thermodynamic properties in Ta. We have shown that the anharmonic free-energy component in the bcc solid can have a significant 15%–20% effect on thermal expansivity, the Grüneisen parameter, and melt temperatures. We have further shown that the electron-thermal free-energy component can similarly affect the specific heat and thermal expansivity in both the solid and the liquid, while only minimally lowering the bcc and fcc melt curves by 3% or less.

We conclude that the present generalized RSMD free-energy method is an attractive approach for calculating accurate multiphase equations of state and equilibrium phase lines,

as well as for investigating metastable phases and possible polymorphism, in weak-coupling materials, provided reliable temperature-independent ion forces are available. Regarding additional stable or metastable solid phases in Ta, the present method can be applied with multi-ion MGPT potentials to the A15 and hcp phases considered in Ref. [12] as well as to the orthorhombic *Pnma* phase suggested by Yao and Klug [17] and by Liu *et al.* [18]. In addition to treatment with MGPT potentials, the present free-energy method can also be adapted to other temperature-independent potentials, including GPT, BOP, EAM, and FS potentials among others, for suitable applications in relevant materials. It may also be possible to extend this method to DFT quantum simulations like QMD in weak-coupling materials, provided the electrons are held at zero temperature and not allowed to equilibrate with the ions, as is normally the case in current QMD simulations on metals. A major challenge there, however, would be the severe limitations on time step and simulation duration imposed by QMD.

ACKNOWLEDGMENTS

This work was performed under the auspices of the U.S. Department of Energy by Lawrence Livermore National Laboratory under Contract No. DE-AC52-07NA27344. J.B.H. acknowledges support as a summer student at LLNL in 2011 from DOE SciDAC Grant No. DE-FC02-06ER25788, during which time some of this work was begun.

[1] D. Frenkel and B. Smit, *Understanding Molecular Simulation* (Academic Press, San Diego, 1996).
[2] M. E. Tuckerman, *Statistical Mechanics: Theory and Molecular Simulation* (Oxford University Press, Oxford, 2010).
[3] M. de Koning, A. Antonelli, and S. Yip, Phys. Rev. Lett. **83**, 3973 (1999), and references therein.
[4] N. W. Ashcroft and D. Stroud, in *Solid State Physics*, edited by F. Seitz, D. Turnbull, and H. Ehrenreich (Academic Press, New York, 1978), Vol. 33, p. 1, and references therein.
[5] D. Alfè, M. J. Gillan, and G. D. Price, J. Chem. Phys. **116**, 6170 (2002).
[6] M. de Koning, A. Antonelli, and S. Yip, J. Chem. Phys. **115**, 11025 (2001).
[7] J. A. Moriarty, Phys. Rev. B **42**, 1609 (1990).
[8] J. A. Moriarty, Phys. Rev. B **49**, 12431 (1994).
[9] J. A. Moriarty, J. F. Belak, R. E. Rudd, P. Söderlind, F. H. Streitz, and L. H. Yang, J. Phys.: Condens. Matter **14**, 2825 (2002).
[10] J. A. Moriarty, L. X. Benedict, J. N. Glosli, R. Q. Hood, D. A. Orlikowski, M. V. Patel, P. Söderlind, F. H. Streitz, M. Tang, and L. H. Yang, J. Mater. Res. **21**, 563 (2006).
[11] J. A. Moriarty, J. N. Glosli, R. Q. Hood, J. E. Klepeis, D. A. Orlikowski, P. Söderlind, and L. H. Yang, in *TMS 2008 Annual Meeting Supplemental Proceedings Volume I: Materials Processing and Properties* (TMS, Warrendale, PA, 2008), p. 313.
[12] J. B. Haskins, J. A. Moriarty, and R. Q. Hood, Phys. Rev. B **86**, 224104 (2012). Reference 33 in this article is the present paper.
[13] A. B. Belonoshko, N. V. Skorodumova, A. Rosengren, and B. Johansson, Phys. Rev. B **73**, 012201 (2006).
[14] J. R. Morris, C. Z. Wang, K. M. Ho, and C. T. Chan, Phys. Rev. B **49**, 3109 (1994).
[15] S. Taioli, C. Cazorla, M. J. Gillan, and D. Alfè, Phys. Rev. B **75**, 214103 (2007).
[16] L. Burakovsky, S. P. Chen, D. L. Preston, A. B. Belonoshko, A. Rosengren, A. S. Mikhaylushkin, S. I. Simak, and J. A. Moriarty, Phys. Rev. Lett. **104**, 255702 (2010).
[17] Y. Yao and D. D. Klug, Phys. Rev. B **88**, 054102 (2013).
[18] Z.-L. Liu, L.-C. Cai, X.-L. Zhang, and F. Xi, J. Appl. Phys. **114**, 073520 (2013).
[19] J. A. Moriarty and A. K. McMahan, Phys. Rev. Lett. **48**, 809 (1982); A. K. McMahan and J. A. Moriarty, Phys. Rev. B **27**, 3235 (1983).
[20] J. A. Moriarty, Phys. Lett. A **131**, 41 (1988).
[21] J. D. Althoff, P. B. Allen, R. M. Wentzcovitch, and J. A. Moriarty, Phys. Rev. B **48**, 13253 (1993); J. A. Moriarty and J. D. Althoff, *ibid.* **51**, 5609 (1995); C. W. Greeff and J. A. Moriarty, *ibid.* **59**, 3427 (1999).
[22] J. A. Moriarty, High Pressure Res. **13**, 343 (1995).
[23] J. A. Moriarty and M. Widom, Phys. Rev. B **56**, 7905 (1997).
[24] D. G. Pettifor, Phys. Rev. Lett. **63**, 2480 (1989).
[25] D. G. Pettifor, *Bonding and Structure of Molecules and Solids* (Oxford University Press, Oxford, 1995).
[26] M. W. Finnis, *Interatomic Forces in Condensed Matter* (Oxford University Press, Oxford, 2003), pp. 242–252.
[27] J. A. Moriarty, R. Q. Hood, and L. H. Yang, Phys. Rev. Lett. **108**, 036401 (2012).
[28] M. S. Daw, S. M. Foiles, and M. I. Baskes, Mater. Sci. Rep. **9**, 251 (1993).
[29] M. W. Finnis and J. E. Sinclair, Philos. Mag. A **50**, 45 (1984).
[30] D. A. Young and F. J. Rogers, J. Chem. Phys. **81**, 2789 (1984).
[31] D. B. Boercker and D. A. Young, Phys. Rev. A **40**, 6379 (1989).
[32] J. A. Moriarty, Phys. Rev. B **38**, 3199 (1988).
[33] L. H. Yang, P. Söderlind, and J. A. Moriarty, Philos. Mag. A **81**, 1355 (2001).
[34] P. Vinet, J. H. Rose, J. Ferrante, and J. R. Smith, J. Phys.: Condens. Matter **1**, 1941 (1989), and references therein.
[35] W. G. Hoover, A. J. C. Ladd, and B. Moran, Phys. Rev. Lett. **48**, 1818 (1982); D. J. Evans, J. Chem. Phys. **78**, 3297 (1983).
[36] M. P. Allen and D. J. Tildesley, *Computer Simulation of Liquids* (Oxford University Press, Oxford, 1989).
[37] W. G. Hoover, *Computational Statistical Mechanics* (Elsevier, Amsterdam, 1991).
[38] P. Söderlind and J. A. Moriarty, Phys. Rev. B **57**, 10340 (1998).
[39] A. D. B. Woods, Phys. Rev. **136**, A781 (1964).
[40] K. W. Katahara, M. H. Manghnani, and E. S. Fisher, J. Phys. F: Met. Phys. **9**, 773 (1979).
[41] C. Bercegeay and S. Bernard, Phys. Rev. B **72**, 214101 (2005).
[42] R. E. Cohen and O. Gülseren, Phys. Rev. B **63**, 224101 (2001).
[43] R. Hultgren, P. D. Desai, D. T. Hawkins, M. Gleiser, K. K. Kelley, and D. D. Wagman, *Selected Values of the Thermodynamical Properties of the Elements* (American Society for Metals, Metals Park, Ohio, 1973), pp. 490–495.
[44] J. W. Shaner, G. R. Gathers, and C. Minichino, High Temp.-High Pressures **9**, 331 (1977).

[45] G. R. Gathers, Int. J. Thermophys. **4**, 149 (1983). This paper corrects pyrometry calibration errors on the liquid temperatures reported in Ref. [44].
[46] A. Berthault, L. Arles, and J. Matricon, Int. J. Thermophys. **7**, 167 (1986).
[47] Y. S. Touloukian, R. K. Kirby, R. E. Taylor, and P. D. Desai, *Thermophysical Properties of Matter (Thermal Expansion: Metallic Elements and Alloys*), Vol. 12 (Plenum, NewYork, 1975).
[48] A. Strachan, T. Cagin, O. Gülseren, S. Mukherjee, R. E. Cohen, and W. A. Goddard III, Modeling Simul. Mater. Sci. Eng. **12**, S445 (2004).
[49] A. Dewaele, M. Mezouar, N. Guignot, and P. Loubeyre, Phys. Rev. Lett. **104**, 255701 (2010).
[50] J. M. Brown and J. W. Shaner, in *Shock Waves in Condensed Matter-1983*, edited by J. R. Asay, R. A. Graham, and G. K. Straub (Elsevier, Amsterdam, 1984), pp. 91–94.
[51] C. Dai, J. Hu, and H. Tan, J. Appl. Phys. **106**, 043519 (2009).
[52] H. Cynn and C.-S. Yoo, Phys. Rev. B **59**, 8526 (1999).
[53] A. Dewaele, P. Loubeyre, and M. Mezouar, Phys. Rev. B **70**, 094112 (2004).
[54] A. C. Mitchell and W. J. Nellis, J. Appl. Phys. **52**, 3363 (1981).
[55] N. C. Holmes, J. A. Moriarty, G. R. Gathers, and W. J. Nellis, J. Appl. Phys. **66**, 2962 (1989).